

## Research Article

# Simple One-Step Leaf Extract-Assisted Preparation of $\alpha$ - $\text{Fe}_2\text{O}_3$ Nanoparticles, Physicochemical Properties, and Its Sunlight-Driven Photocatalytic Activity on Methylene Blue Dye Degradation

V. Archana <sup>1</sup>, J. Joseph Prince <sup>1</sup>, and S. Kalainathan <sup>2</sup>

<sup>1</sup>Department of Physics, University College of Engineering, Anna University-BIT Campus, Tiruchirappalli 620024, Tamil Nadu, India

<sup>2</sup>Centre for Nanotechnology Research, VIT, Vellore, Tamil Nadu 632014, India

Correspondence should be addressed to V. Archana; [c.v.archanavenkat@gmail.com](mailto:c.v.archanavenkat@gmail.com)

Received 24 July 2020; Revised 26 March 2021; Accepted 29 April 2021; Published 2 June 2021

Academic Editor: Thathan Premkumar

Copyright © 2021 V. Archana et al. This is an open access article distributed under the Creative Commons Attribution License, which permits unrestricted use, distribution, and reproduction in any medium, provided the original work is properly cited.

Hematite nanoparticles have been prepared from *Moringa oleifera* leaf extracts. Phytochemicals are derived from plant extracts which act as a stabilizing and capping agent as well as a surfactant. This green route protocol is attractive owing to its speed, reliability, and ecofriendly and cost-effective qualities. The synthesized iron oxide nanoparticles were subjected to three different calcination temperatures (500, 600, and 700°C). The crystallinity nature and phase purity have been confirmed by powder X-ray diffraction (PXRD). Optical properties have been studied by UV-visible (UV-vis) and diffuse reflectance spectroscopy (DRS). A very narrow bandgap was observed, and absorbance was observed at the visible region. Photoluminescence spectra have exhibited a multicolor emission band from the near UV to visible region due to defect centers (F centers). EDX (energy dispersive X-ray spectrum) has given information on the stoichiometric ratio of Fe and O. The functional groups which are responsible for nanoparticle formation have been identified by Fourier transformed infrared spectroscopy (FTIR), surface morphology transformation has been illustrated by scanning electron microscopy (SEM) studies, and VSM measurements have exhibited a hysteresis curve that shows the weak and strong ferromagnetic behavior in nature at RT. TEM micrographs have confirmed that particles are in the nanorange, matching the results from the XRD report. The SAED pattern gives information on the polycrystalline nature of hematite nanoparticles. TG-DSC characterization revealed phase transition, decomposition, and weight loss information. Frequency-dependent electrical properties were studied. Here, we report what the present studies have revealed: that hematite nanopowder prepared from the green route is environmentally friendly, takes a short time to prepare, is an economical and promising candidate material for electromagnetic devices and ferromagnet manufacturing, and is a photocatalyst in water treatment applications without adding additives ( $\text{H}_2\text{O}_2$ ).

## 1. Introduction

Phytochemical-mediated synthesis is a green route protocol that has received great attention because it is a novel strategy and it is an alternative to physical and chemical methods [1]. In this type of bottom-up approach, the phytochemicals reduce the raw materials into metal nanoparticles. The reducing agents involved in nanoparticle synthesis are alkaloids, phenolic compounds, terpenoids, and coenzymes. The bioactive compounds can act as a capping and stabilizing agent [2, 3]. The biosynthesis route employs simple prokary-

otic bacteria and eukaryotes such as fungi and plants. Bio-green synthesis has a greater advantage compared to microorganisms wherein plant-mediated synthesis uses a one-step synthesis. However, because of the mutation of microorganisms over time, they may lose their ability to synthesize nanoparticles; in addition, the process is very laborious and time consuming [4]. Plant-mediated synthesis is a one-step protocol and is safe; hence, research on plants has expanded rapidly [4–6]. As biological agents, plants serve as reducing and capping agents involved in the synthesis process which is considered ecofriendly [7, 8]. Every part of

the plant can be used for nanoparticle synthesis, like the leaves, stems, straws, and flowers [7–13]. The leaf extract acts as an environmental reducing agent that is nonhazardous and nontoxic. Here, extracellular methods had been used for the synthesis of nanoparticles including the use of leaf extract prepared by boiling or crushing leaves [14–16]. There are many advantages when comparing the green method over the chemical method of synthesis, namely, it can be prepared at room temperature, it uses nonpoisonous capping, it functions as a stabilizing agent, it is an easy method, it can be applied for large scale production, and it is economical as well.

Biosynthesis of iron (III) oxide ( $\alpha$ - $\text{Fe}_2\text{O}_3$ ) hematite nanoparticles prepared from *Moringa oleifera* leaf extracts is reported here. When exposed to *Moringa oleifera* leaf extract, aqueous metal ions are reduced and metal and metal oxide nanoparticles are formed. The plant belongs to the Moringaceae family. It is distinguished by parietal placentation; a 3-valved fruit; an elongated, nondehiscent berry; and winged seeds. It is a medium-sized tree, and the botanical name of the tree is *Moringa oleifera* Lam. The family consists of the single genus *Moringa* [17]. It is widely available in India, and it is an essential dietary ingredient in Indian food. The plant contains minerals, protein, vitamins, amino acids, and phenolics and provides a rich and rare combination of zeatin, quercetin,  $\beta$ -sitosterol, caffeoylquinic acid, and kaempferol. The leaves contain concentrations of ascorbic acid; estrogenic substances [18]; iron; calcium; phosphorus; copper; vitamins A, B, and C;  $\alpha$ -tocopherol; riboflavin; nicotinic acid; folic acid; pyridoxine;  $\beta$ -carotene; protein; and in particular, essential amino acids such as methionine, cysteine, tryptophan, and lysine [19]. Nanoparticle synthesis using a plant system is the current scenario. Plant-mediated synthesis is not only used for environmental impact but is also used to produce large quantities of contamination-free nanoparticles with a well-defined morphology and size [20–22]. The characteristics of the nanoparticles have been influenced by the source of the plant extract because different extracts contain different concentrations and combinations of organic reducing agents. A plant extract-mediated bioreduction involves mixing the aqueous extract with an aqueous solution of the relevant metal salt at room temperature, and it can be completed within a few minutes [2, 3, 23, 24]. Various metal nanoparticles have been synthesized from the *Moringa oleifera* leaf extract.

Generally, metal oxides are widely employed as catalysts, optical devices, sensors, thermal conductivity enhancers, energy conversion devices, biomedical imaging, paints, optoelectronic devices, and nanodrug delivery [24–34]. Engineered nanomaterials have unique properties, and their shape, size, and morphology can be tailored leading to outstanding properties which are limited to bulk materials. A variety of differently structured metal oxides include nanoparticles, wires, tubes, fibers, whiskers, films, layers, triangles, tetrapods, disc, and sheets. They are the most desired structures widely used in technical applications, and their unique structural features are large surface-to-volume ratio, cations with valence states, anions with deficiencies, and depletion of carriers [1]. Among all of the metal nanoparticles, iron

oxide has attracted the most attention due to its high economical availability, colloidal stability, nontoxicity, ecofriendly nature, magnetic property, and surface engineering capability, and it can be tailored according to its shape and size [35]. It has been widely used as catalysts, pigments in paint, noncorrosive agents due to its corrosion resistivity, optoelectronic devices, gas sensors, biosensors, and devices for solar energy conversion, water splitting, water purification, and high-density data storage. Because of its magnetic property, it is used as a contrasting agent in biomedical imaging techniques like MRI scans, absorbents, biomedical applications like in *in vitro* and *in vivo* studies, targeted drug delivery, bioseparation, and magnetic fluid hyperthermia. Magnetic iron oxide nanoparticles can easily be conjugated with DNA, peptides, and antibodies. They can be used in anticancer therapy, ferrofluids, cell labeling, and separation, and they show significant physical and chemical properties concerning their oxidation states [35–38]. Nowadays nanobiohybrid particles have been prepared, which both have magnetic and biological functions in biomedical therapeutics and diagnostics.

Iron oxides have multiple forms that are polymorphic in nature. Among them, iron (III) oxide (hematite ( $\alpha$ - $\text{Fe}_2\text{O}_3$ )), magnetite ( $\text{Fe}_3\text{O}_4$ ), and magemite ( $\gamma$ - $\text{Fe}_2\text{O}_3$ ) are common forms [38]. Iron oxides have been synthesized through various synthetic methods including hydrothermal, coprecipitation, sonochemical, sol-gel, thermal decomposition, and wet chemical [1–6]. Here, we synthesized through a one-step simple green route and focused on hematite nanoparticles ( $\alpha$ - $\text{Fe}_2\text{O}_3$ ) alone. Hematite is an n-type semiconductor with a narrow bandgap of 2.2 eV. It exhibits long-term stability under ambient conditions [36]. Owing to its unique chemical, thermal, optical, magnetic, and electrical properties and its high stability in ambient conditions, it has received great attention among researchers. Usually, the hematite nanoparticles are antiferromagnetic in nature, where spins are aligned antiparallel in adjacent planes [37]. But here, the synthesized iron oxide nanoparticles show an unusual ferromagnetism at room temperature, and the prepared nanoparticles by this plant extract-assisted method has yielded large coercivity magnetic iron oxide nanoparticles as illustrated in *M-H* measurements. The hematite nanoparticles prepared by this one-step green protocol will be a promising material in spintronics, data storage devices, ferromagnet manufacturing, and electromagnetic devices owing to their natural RTFM. Hematite nanoparticles have a very narrow bandgap, so they can be used as a visible-light catalyst in wastewater or polluted-water purification. Here, we report a simple, low-cost, ecofriendly, room temperature one-step synthesis protocol for hematite nanoparticle preparation. The prepared hematite nanoparticles were air-dried and heated at different temperatures and chemical and physical properties; then, their various parameters were analyzed by different characterization tools, and the results were summarized and explained. Aqueous *Moringa oleifera* leaf extract-mediated synthesis of hematite nanoparticles exhibited a room temperature ferromagnetism with a rich coercivity value, and it degraded the methylene blue dye in an aqueous solution under visible light. Even though there are many narrow-

FIGURE 1: *Moringa oleifera*.

gap metal oxides that are designed for dye degradation such as  $\text{TiO}_2$ ,  $\text{WO}_3$ , and  $\text{ZnO}$  [39], these are undergoing research and have not gained great attention for the degradation of water pollutants under visible light in an aqueous medium. However, iron (III) oxide has received great attention. The synthesized disc-like hematite nanostructure has degraded 69% of dye under sunlight. So, the reported green preparation of hematite nanoparticles with disc-like morphology promises to be a visible-light photocatalyst for removing organic pollutants in water. The bioactive molecules act as a capping and stabilizing agent in nanoparticle formation, so we can avoid using toxic chemicals to avoid aggregation in nanoparticle formation. Hematite nanoparticles are magnetic, hence they can be used as a magnetic catalyst and could be recovered from the solution with a magnet so it will be reused in the degradation of dyes [21, 22, 40–42]. Herein, we report a simple one-step protocol to produce a nanoparticle with different morphologies and with no surfactant, can act as a stabilizing and capping agent, and is a highly stable magnetic iron oxide with a high coercivity value which could act as an environmentally friendly, biodegradable, magnetically separated magnetic visible-light catalyst to remove organic pollutants in an aqueous medium.

## 2. Materials and Methods

**2.1. Material Collection.** Fresh *Moringa oleifera* leaves were collected from the southern part of Tamil Nadu, India (10.3673°N, 77.9803°E). *Moringa oleifera* leaves were collected from homes, and analytical grade (AR) chemicals were used without further purification.  $\text{FeCl}_3$  and sodium hydroxide pellets (NaOH) were purchased from Alfa Aesar Pvt. Ltd. (purity 98%).

**2.2. Aqueous *Moringa oleifera* Leaf Extract Preparation.** Freshly collected *Moringa oleifera* leaves were washed thoroughly with double-distilled water to remove dust particles, weighed, and transferred into the round bottom flask, and it

was mixed with water and refluxed for 40 minutes at 70 degrees Celsius in a heating mantle. Then, the extract was filtered using Whatman filter paper (No. 1) several times and kept in sterile bottles under refrigerated conditions for future use. The leaf and its extract are shown in Figures 1(a) and 1(b).

**2.3. Preparation of Leaf Extract-Assisted Hematite ( $\alpha\text{-Fe}_2\text{O}_3$ ) Nanoparticles.** Freshly prepared *Moringa oleifera* leaf extract (stabilizing agent and capping agent as well) was added drop by drop to 100 ml of an aqueous solution of  $\text{FeCl}_3$  and stirred vigorously at room temperature. Then, a few drops of NaOH were added into the homogeneous solution under stirring to maintain an appropriate pH; it acts as a precipitating agent as well. The pale red color of the solution changed into a dark brown color after 4 hrs of stirring; then, the precipitation settled at the bottom of the flask as dark brown colloidal particles. The dark brown color indicates the formation of hydrated iron nanoparticles and is shown in Figure 2(a). The colloidal solution was then centrifuged several times at a speed of 4000 rpm for 15 minutes in the centrifuge machine and then washed several times with double-distilled water and ethanol to remove the loosely bounded impurities. After the washing process was over, the supernatant was collected and dried overnight in a hot air oven at 70 degrees Celsius. The dried dark brown samples were collected, crushed, and ground by mortar and pestle. The ground samples were calcinated in a muffle furnace at three different temperatures of 500, 600, and 700°C for three hours for dehydration. This process removes the organic and other impurities, until finally, a deep-red-colored iron oxide nanopowder is obtained and is shown in Figures 2(b) and 2(c). The dried samples were submitted to different characterization techniques to study the physical and chemical properties. The formation mechanism of  $\alpha\text{-Fe}_2\text{O}_3$  is shown in Figure 2(d).

**2.4. Formation Mechanism of  $\alpha\text{-Fe}_2\text{O}_3$**

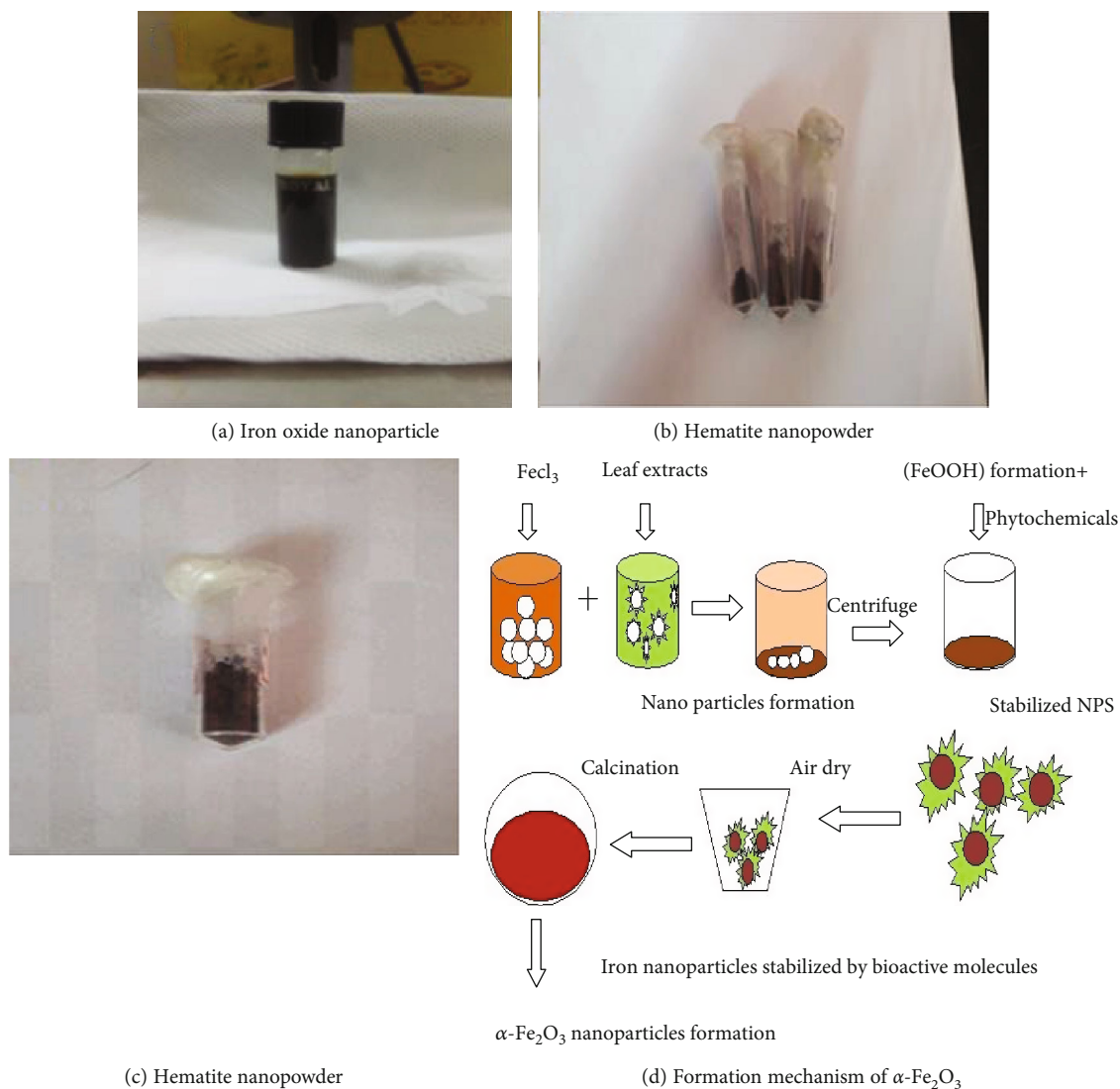
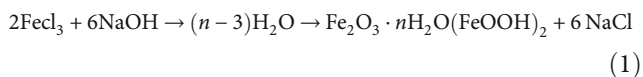


FIGURE 2: Hematite nanopowder prepared from *Moringa oleifera* leaf extract.

- (a) The role of precipitating agents in hematite nanoparticle formation is



- (b) The role of phytochemicals in hematite nanoparticle formation is to serve as capping and stabilizing agents

**2.5. Material Characterization and Instrumentation.** The calcinated iron oxide nanoparticles were analyzed with the PANalytical X' Pert Pro Powder X-ray Diffractometer with  $\text{CuK}\alpha$  radiation operated at 40 kV and 30 mA and with a wavelength of  $\lambda = 1.54060 \text{ \AA}$  in the range of  $2\theta = 10 - 80^\circ$ . The photoluminescence spectra studied with the 300–700 nm regions were recorded with a Varian Cary Eclipse

photoluminescence spectrophotometer at room temperature with an excitation wavelength of 320 nm. UV-visible spectroscopic studies were conducted with a Shimadzu dual-beam spectrometer. The size of the nanoparticle was determined by a transmission electron microscope (FEI Tecnai T20) accelerated at 200 kV, the morphology of the hematite nanoparticles was studied using a scanning electron microscope (JEOL JSM-6390), and elemental analysis was performed by energy dispersive X-ray analysis (EDS) which is attached to an SEM X-ray column along with SEM images of nanoparticles. The functional groups were found using a Fourier transform infrared spectrum (FTIR) spectrophotometer (Perkin Elmer Spectrometer) using KBr pellets in the spectral range of  $4000-400 \text{ cm}^{-1}$ . Investigation of magnetic properties was performed at room temperature, where a vibrating sample magnetometer model is employed, and here, the applied magnetic field ranged from  $-15000$  to  $+15000$  (Lakeshore, USA, model 740 equipped with a 2.17 T magnetic field). Thermal properties were analyzed by the thermal analyzer NETZSCH STA 449 F3 Jupiter which performs simultaneous

TG-DSC measurement on the sample. Dielectric properties were characterized by an a.c. impedance spectroscopy and dielectric analysis using the Hioki 3532-50 LCR HiTESTER meter in the frequency range of 50 Hz–5 MHz.

**2.6. Photocatalytic Studies.** To examine the photocatalytic activity of the prepared samples, the methylene blue dye was taken as a pollutant, and sunlight was used as a light source. 50 ml of 10 ppm dye solution was taken, and 0.5 mg of the prepared photocatalyst was used. This experiment was performed on a perfect sunny day, and the time was between 12 pm and 2 pm. The aliquots of dye solution were taken every 20 min and subjected to UV-vis spectroscopy to analyze the change in concentration of the solution. The degradation efficiency was calculated using the following:

$$\eta = \frac{1 - C}{C_0} \times 100(\%). \quad (2)$$

### 3. Results and Discussion

**3.1. Structural Analysis.** Phase purity, crystal structure, and crystallinity conformed with powder X-ray diffraction (PXRD) techniques. The synthesized IONPs (iron (III) oxide nanoparticles) were calcined at three different temperatures (500, 600, and 700°C) at a muffle furnace. After air drying in a hot air oven, it was characterized with PXRD. The diffraction patterns are shown in Figure 3. At 500°C, no peak was observed, which implies that the sample calcined at 500°C was amorphous in nature, and there was no growth. The peaks were observed to have a diffraction pattern with poor crystallinity when the IONPs were calcined at a 600°C calcination temperature, whereas the peaks were observed with good crystallinity when they were calcined at 700°C. The IONPs calcined at 600 and 700°C temperatures have a pure hematite phase ( $\alpha$ -Fe<sub>2</sub>O<sub>3</sub>), and it belongs to the rhombohedral crystal structure with the R-3c space group. The space group number is 167 and is affirmed by diffraction peaks which are illustrated in Figure 3. The lattice constant values are  $a = 5.0285 \text{ \AA}$ ,  $b = 5.0285 \text{ \AA}$ ,  $c = 13.7360 \text{ \AA}$ . All peaks were indexed according to ICDD reference number 01-079 0007. The XRD patterns clearly show that there are no additional peaks belonging to other phases of the iron oxides ( $\beta$ -Fe<sub>2</sub>O<sub>3</sub>,  $\epsilon$ -Fe<sub>2</sub>O<sub>3</sub>, and  $\gamma$ -Fe<sub>2</sub>O<sub>3</sub>) and magnetite (Fe<sub>3</sub>O<sub>4</sub>). Hence, pure  $\alpha$ -Fe<sub>2</sub>O<sub>3</sub> hematite nanoparticles have been formed through this single-step biogenic synthesis.

Debye-Scherrer's formula was employed to calculate the average crystallite size of IONPs as shown below:

$$D = \frac{K \cdot \lambda}{\beta \cos \theta}, \quad (3)$$

where  $K$  is the shapeless factor,  $\lambda$  is the X-ray wavelength for CuK $\alpha$  radiation (1.5406 Å),  $D$  is crystallite size,  $\theta$  is Bragg's diffracting angle,  $\beta$  is full-width half maximum (FWHM) strain broadening. Calculated crystallite size is shown in Table 1. The crystallite size has increased with rising heat treatment. The trend of a linearly increasing crystallite size with temperature is matched with the previous reports.

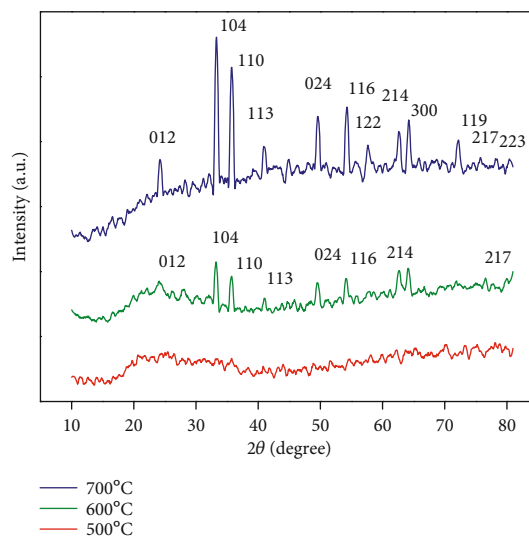


FIGURE 3: PXRD patterns of hematite nanoparticles at 500°C, 600°C, and 700°C.

TABLE 1: Crystallite size and lattice strain.

Temperature	Average crystallite size(D) (nm)	
	Debye-Scherrer's method	Lattice strain W-H ( $\times 10^{-3}$ ) (UDM model)
500°C	—	—
600°C	23	-10.5
700°C	35	3.55

#### 3.2. Lattice Microstrain Calculation

**3.2.1. W-H Plot Method with UDM (Uniform Deformation Model).** The microstrain of the hematite nanopowder was found by the William-Hall method. Let it be considered that the strain is uniform in all crystallographic directions due to the isotropic nature of crystals.

The lattice microstrain can be estimated from the following formalism:

$$\beta \cos \theta = \frac{K \cdot \lambda}{D} + (4\epsilon \sin \theta), \quad (4)$$

where  $\beta$  is strain broadening,  $K$  is the dimensionless shape factor (0.9),  $\epsilon$  is the lattice strain,  $D$  is the crystallite size,  $\lambda$  is the X-ray wavelength for the CuK $\alpha$  radiation (1.5406 Å), and  $\theta$  is Bragg's diffracting angle.

$\beta \cos \theta$  values were taken from the y-axis, and  $4 \sin \theta$  values were taken from the x-axis, respectively. Then, fitted linearly from the slope (gradient) value, the lattice strain was calculated. Owing to the existence of the tensile strain and compression on the lattice, the positive and negative slopes (strain) were observed from the W-H plot. The calculated strain is shown in Table 1, and the W-H plot is shown in Figure 4.

**3.3. Surface Morphology, Size of the Particle, and Elemental Composition Analysis.** The particle dispersion, crystallinity,

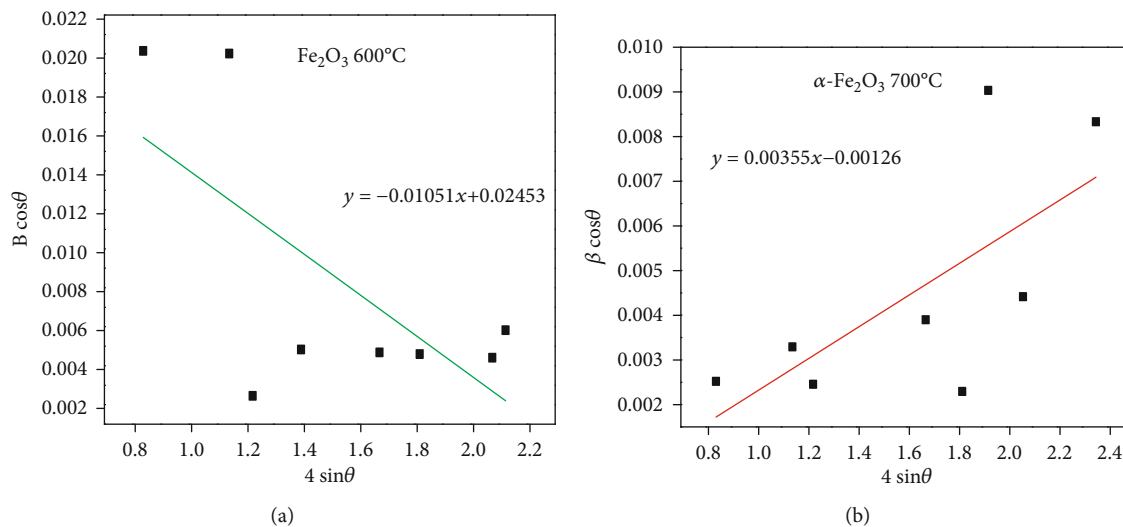


FIGURE 4: William-Hall's plot of  $\alpha\text{-Fe}_2\text{O}_3$  at  $600^\circ\text{C}$  (a) and  $700^\circ\text{C}$  (b).

morphology, and size were observed from SEM (scanning electron microscope) and TEM (transmission electron microscope) imaging techniques. SEM micrographs are shown in Figure 5. In the air-dried samples that were calcined at  $500^\circ\text{C}$ , all the particles were aggregated and it seems that there was a sheet-like morphology as observed in Figures 5(a) and 5(b). In samples that were calcined at  $600^\circ\text{C}$ , a nanoplate-like morphology was formed as shown in Figures 5(c) and 5(d), and it started to grow and a clear hexagonal nanodisc morphology was observed at  $700^\circ\text{C}$  as shown in Figures 5(e) and 5(f). A temperature-dependent morphology was observed from the SEM micrographs, and it was clearly seen to be regular and clustered, with clear shapes that could be observed. Shape transformation was a function of calcination temperatures and could be a reason for yielding high-crystallinity IONPs..

In order to confirm the morphology, the size of the particle, and the nature of crystallinity of the nanostructured hematite particles, TEM imaging techniques and SAED (selected area electron diffraction) pattern analysis were employed. The bright field images of TEM of the samples are shown in Figure 6. The sample was annealed at  $500^\circ\text{C}$ , and a sheet-like morphology can be seen in Figures 6(a) and 6(b). At  $600^\circ\text{C}$  and  $700^\circ\text{C}$ , the hematite nanoparticles have exhibited nanoplate-like morphology and hexagonal nanodisc morphology as illustrated in Figures 6(c)–6(f). To further confirm the crystallinity of IONPs, SAED pattern analysis was employed. The SAED micrographs of the hematite nanoparticles are shown in Figure 6. The sample that was calcined at  $500^\circ\text{C}$  has only diffuse rings, and no bright spots were observed at the diffraction pattern. So we conformed that the sample is amorphous in nature, as shown in Figure 6(g). The SAED patterns of samples which were annealed at  $600^\circ\text{C}$  and  $700^\circ\text{C}$  have discrete tiny bright and sharp spots which make up the ring. This implies that the IONPs are crystalline in nature, as shown in Figures 6(h) and 6(i). This is in conformity with the TEM micrographs showing all the

particles are nano in size, and this is in good agreement with XRD reports.

The elemental concentration of hematite nanoparticles that was determined from the EDX spectrum is shown in (Figure 7(a)). The EDX spectrum confirmed that it has only Fe and O elements. The obtained atomic percentage of Fe and O was clearly tabulated and indicated as an inset in the EDX spectra (Figure 7(b)). It was also observed that it has a good stoichiometric ratio of Fe and O.

**3.4. Optical Properties.** Absorbance and diffuse reflectance spectra of hematite nanoparticles have been discussed, and their optical properties have been reported here. The electronic transitions occur in iron oxide nanoparticles because they are magnetically coupled and exhibit ligand-to-metal charge transfer (LMCT). These are the origins for the electronic transition within the shell of the  $3d^5$  orbital of  $\text{Fe}^{3+}$  ions and could be the reason why the absorption bands are exhibited in iron oxides from UV to near IR wavelengths. First,  $\text{Fe}^{3+}$  cations appear in adjacent sites which are magnetically coupled. Secondly, ligand field transitions of  $\text{Fe}^{3+}$  occur, and then there is charge transfer from ligand to metal (LMCT). The double excitation process is the reason for the bands appearing in the visible region. This means that excitation occurs within two adjacent Fe ions or a pair of  $\text{Fe}^{3+}$  ions. This process yields the absorption band at the visible region, so the hematite color is red. The transition process from  ${}^6\text{A}_1({}^6\text{S}) + 6\text{A}_1({}^6\text{S})$  to  ${}^4\text{T}_1({}^4\text{G}) + {}^4\text{T}_1({}^4\text{G})$  occurs due to a pair of excitation processes, so the band is absorbed at the visible region (400–600 nm) [43, 44].

**3.5. Absorbance Spectrum and Band Gap Calculation (before Calcination).** UV-vis absorbance spectroscopy explains the optical property and electronic structure of the nanoparticles. The UV-visible absorption spectrum and Tauc plot of hematite nanoparticles is shown in Figures 8(a) and 8(b). It was taken once the nanoparticles were formed, that is, before

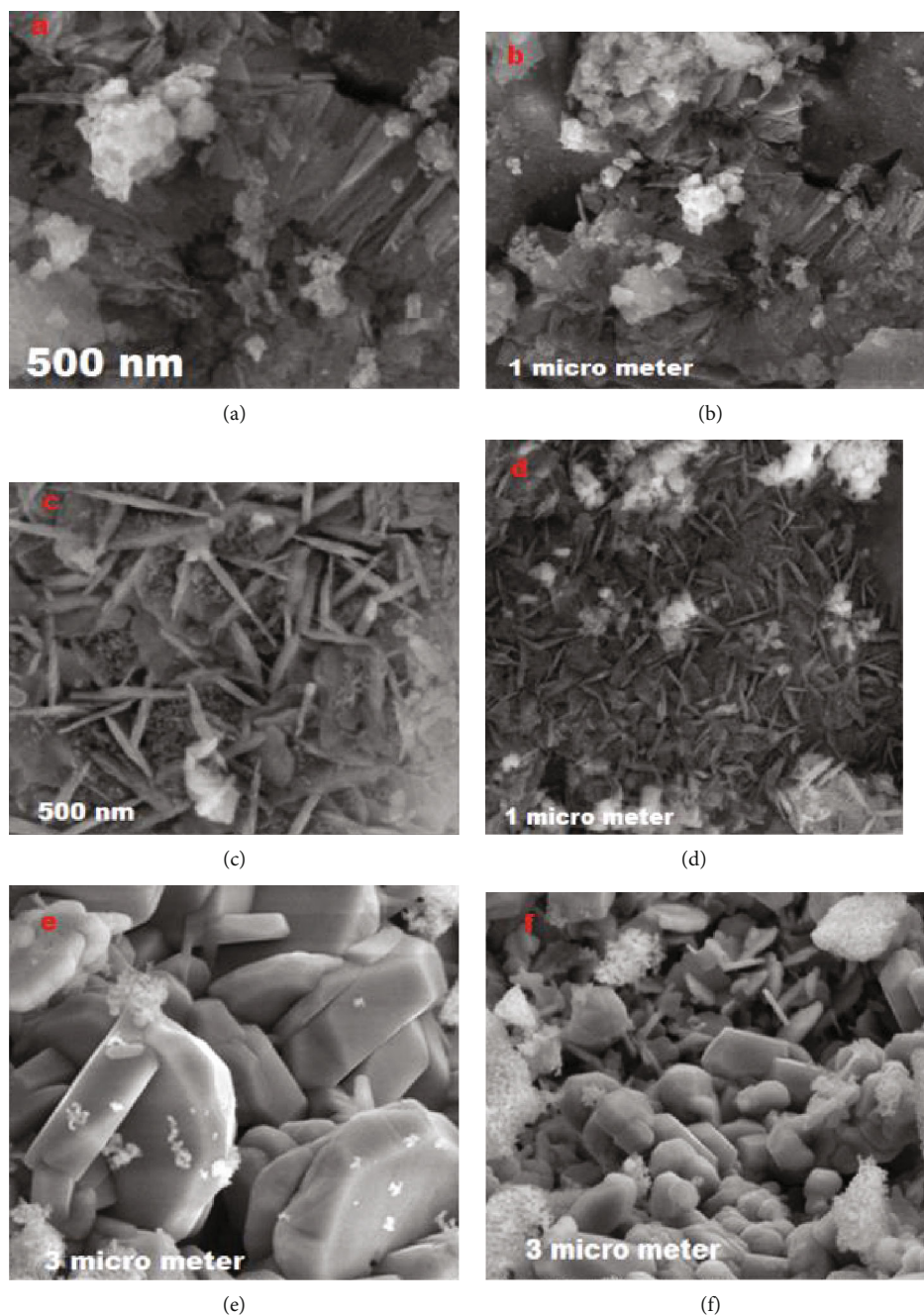


FIGURE 5: SEM images of hematite nanoparticles at 500°C (a, b), 600°C (c, d), and 700°C (e, f).

calcination. The absorbance spectrum was recorded in the range of 200 nm to 800 nm. The absorption band edge was found at 459 nm in the visible region, and the energy band gap value is 2.7 eV. The optical band gap ( $E_g$ ) value was computed from the Tauc plot using the following:

$$\alpha = \frac{A(h\nu - E_g)^n}{h\nu}, \quad (5)$$

where  $\alpha$  is the absorption coefficient,  $E_g$  is the optical band gap of the hematite nanoparticles,  $A$  is a constant,  $h\nu$  is the energy of the photon,  $n$  is the nature of transitions.

**3.6. DRS Spectrum and Band Gap Calculation (after Calcination).** The optical properties of hematite nanoparticles were studied from the reflectance spectrum, and they were analyzed by diffuse reflectance spectroscopy (DRS). It was done after calcination of the samples. It was recorded in the range of 200 nm to 800 nm in reflectance mode. The optical band gap energy of hematite nanoparticles was calculated by the Kubelka-Munk function:

$$F(R) = \frac{(1 - R)^2}{2R}, \quad (6)$$

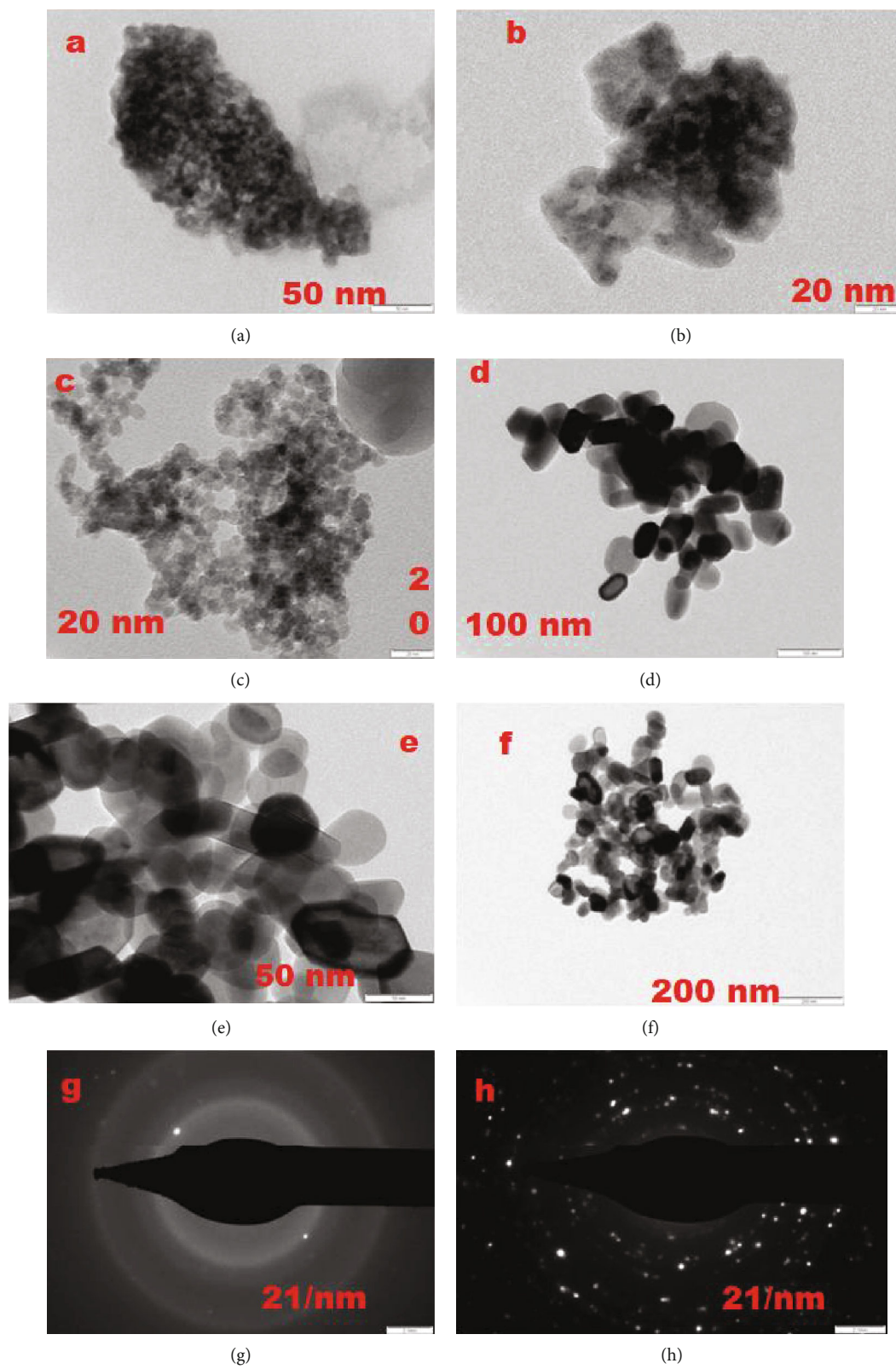


FIGURE 6: Continued.



(i)

FIGURE 6: TEM images and SAED patterns of hematite nanoparticles at 500°C (a, b, and g), 600°C (c, d, and h), and 700°C (e, f, and i).

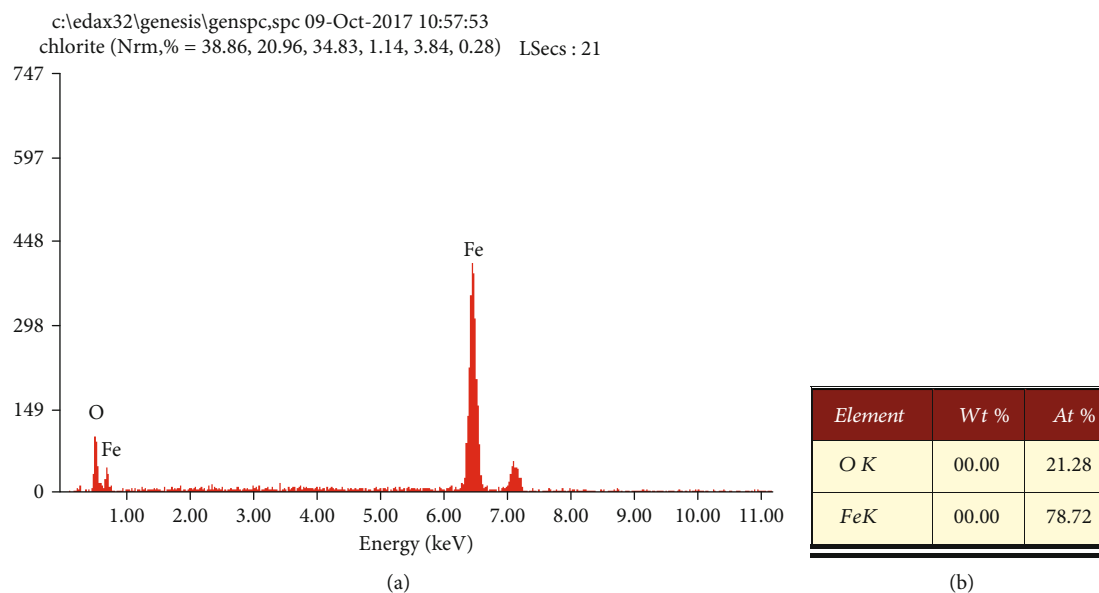


FIGURE 7: EDX spectra of hematite nanoparticles (a) and atomic percentage of Fe and O (b).

where  $R$  is reflectance. The graph was plotted between  $(F(R)hv)^2$  and  $hv$ . The energy band gap values at different calcination temperatures have been calculated by extrapolation of the linear part of  $(F(R)hv)^2$  at the  $x$ -axis plot to the intersection with  $hv$  at the  $y$ -axis. The intercept value is the energy band gap of hematite nanoparticles. The calculated  $E_g$  values of 1.7 eV, 1.5 eV, and 1.2 eV for 500, 600, and 700°C are illustrated in the KM plot, as shown in Figure 8(c). The band gap value has decreased when increasing temperature was observed owing to the growth of particles and crystallinity, and the value matches well with previous reports [1]. The smallest band gap was observed when calcined at 700°C [45–49]. A significant blue shift was observed owing to a quantum confinement effect [50].

**3.7. Functional Group Analysis.** The FTIR spectrum of hematite nanoparticles is shown in Figure 9. FTIR analysis is a tool used to identify the functional groups which are responsible for the formation of metal oxides in plant leaf extract-mediated synthesis. The FTIR spectrum was recorded at the wave number of 400–4000  $\text{cm}^{-1}$ . *Moringa oleifera* leaf

extract FTIR spectra exhibit four intense peaks centered at 3433  $\text{cm}^{-1}$ ; 3452  $\text{cm}^{-1}$ , attributed to –OH stretching vibrations; and a peak at 1636  $\text{cm}^{-1}$  assigned to –OH bending vibrations owing to contamination of the sample during analysis or ambient water molecules or signal distortions [51–53]. The band observed at 1034  $\text{cm}^{-1}$  corresponds to the aromatic stretching of various bioactive compounds and proteins [54, 55]. None of the peaks was observed at 2900  $\text{cm}^{-1}$  since the phytochemicals had been removed during the calcination process. The transformation from an enol form to a keto form is due to the presence of flavonoids and phenols. This mechanism reduces the metal ions and forms nanoparticles since it releases reactive H atoms and forms the O–H group since the phenol group has an electron-donating ability [55, 56]. The metal oxide characteristic absorption band arises from below 1000  $\text{cm}^{-1}$  to form interatomic vibrations. The peak observed at 431  $\text{cm}^{-1}$  indicates the presence of  $\text{Fe}_2\text{O}_3$ ; moreover, the peaks were present at 958  $\text{cm}^{-1}$  and 651  $\text{cm}^{-1}$  attributed to the Fe–O stretching and Fe–O–Fe bridging stretching modes [53, 56, 57]. Then, FTIR analysis results were used to identify the functional

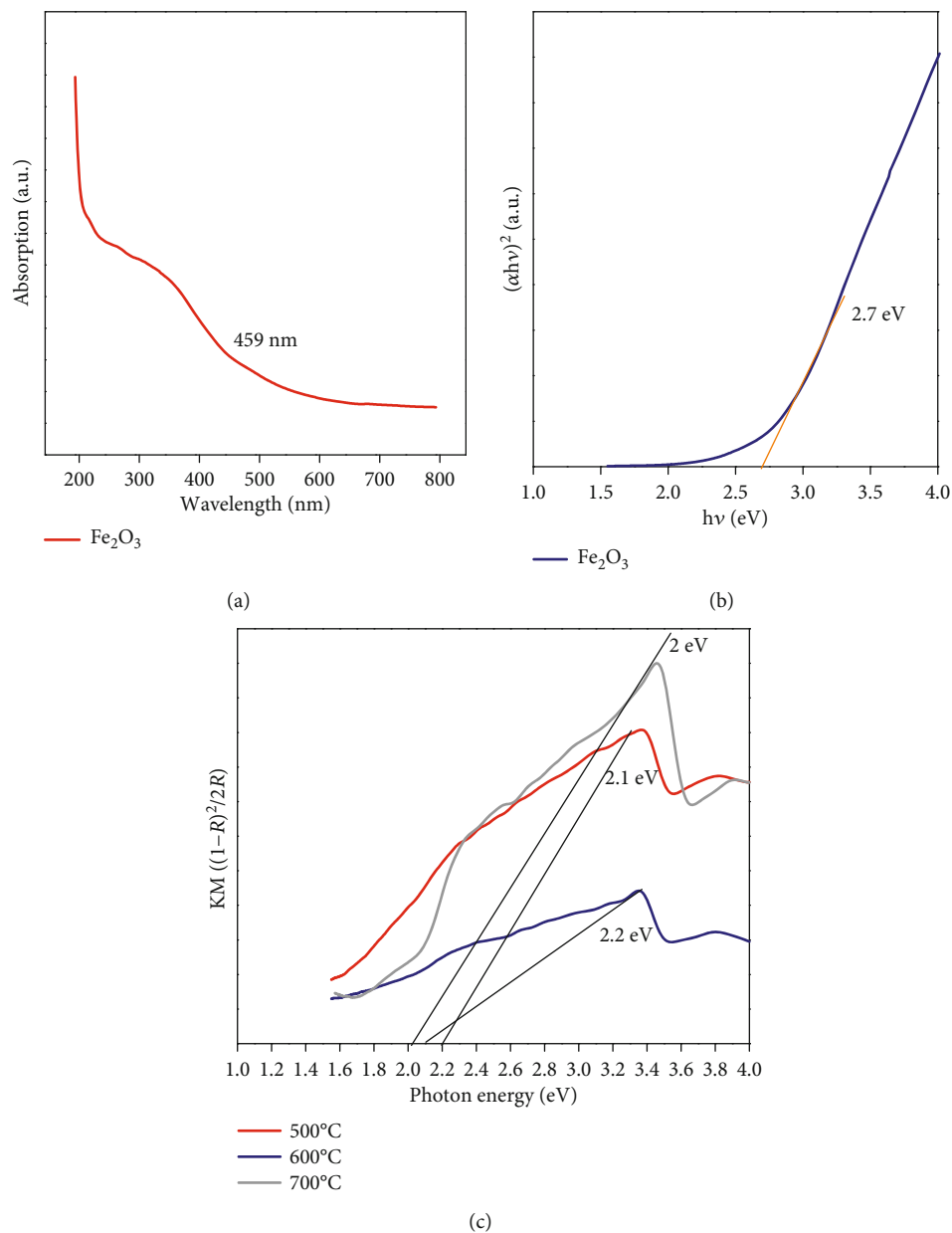


FIGURE 8: Absorption spectra and Tauc plot (a, b) and KM plot of diffuse reflectance spectra (c).

groups and phytochemicals which are responsible for stabilizing and reducing hematite nanoparticles.

**3.8. Thermal Analysis (TG, DTA, and DSC).** Thermal analysis of hematite nanoparticles has been carried out from room temperature to 1200°C. The sample to be analyzed is placed on an alumina crucible, and the samples are heated in an air atmosphere at the range of 10°C/min. The TGA/DTA and DSC thermographs of the nanoparticles are shown in Figure 10. The synthesis is the green mediated one so the phytochemicals were conjugated with hematite nanoparticles so it will be removed during the heat treatment. We can confirm this one from weight loss information from the TGA curve. The weight loss information and the exothermic and endothermic peaks were studied from the TGA/DTA ther-

mograph. The first weight loss takes place due to the OH groups present at the surface, so water molecules have been removed. The second weight loss is due to the phytochemicals present in the hematite nanoparticles which evaporated. And the third weight loss is due to the formation of a completely pure  $\alpha\text{-Fe}_2\text{O}_3$  phase [58–60]. The endothermic peaks were observed at the DTA thermograph at 286, 916, and 910°C temperatures. The peaks were obtained in the DSC thermograph due to the evaporation of water and organic substances and crystallization of iron oxide [58–60].

**3.9. Surface Defect Analysis (Photoluminescence Properties).** The room temperature photoluminescence property of hematite nanoparticles has been studied to elucidate the surface defects, to study the quantum size effect, and to explore

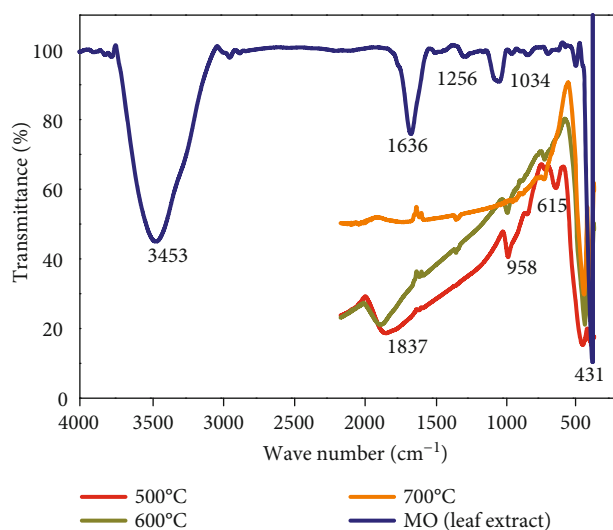


FIGURE 9: FTIR spectra of hematite nanoparticles and *Moringa oleifera* leaf extract.

the optical properties. The possible emission band is shown in photoluminescence spectra for all the samples obtained at different calcination temperatures. The PL spectra were recorded at room temperature with a xenon lamp as an excitation light source. The hematite nanoparticles that were excited with the 320 nm wavelength and the emission spectra that were recorded are shown in Figure 11. The bulk hematite nanoparticles do not show the photoluminescence emission because of forbidden  $d-d$  transition, magnetic relaxation, and an efficient lattice [44, 61, 62]. The magnetic nanoparticles have quantum confinement effects so electronic states of a nanometal oxide relax the forbidden rule in  $d-d$  transition, and partial optical transition is allowed so it exhibits the PL spectra [44]. Nanostructured metal oxides have a high surface-to-volume ratio, so they have a large surface area associated with defects and they create more oxygen vacancies. Because they have a large surface area, nanomaterials have dangling bonds [62]. Generally, holes from the valence band and electrons from the electronic states are recombined with each other; this is responsible for the emission, that is, electronic transition behavior occurs within the transition metals. The emission band originates from the quantum confinement effect and the influence of particle size [62]. PL spectra in hematite nanoparticles cover a broad range from UV to near the orange visible region. The hematite nanoparticles have a multicolor emission peak from near UV to the orange color band in the visible region (363 nm–592 nm) in all the samples due to surface modification. There is a multicolor emission band observed in various regions. The near UV emission band is centered at 363 nm (3.41 eV), the violet band at 405 nm (3.0 eV), the green band at 521–544 nm, and the orange band at 592 nm wavelengths, respectively. The first peak is observed at 363 nm (3.41 eV) owing to the recombination of holes and electrons and is attributed to exciton emission, and the last peak is a weak band observed at 592 nm and attributed to band edge transition owing to defects at the forbidden energy region and  $\text{Fe}^{3+}$  ligand field transition [44, 61, 62]. The violet

emission band is centered at the 404 nm wavelength (3 eV) due to  $\text{F}^+$  (or  $\text{V}_{\text{O}}^{+1}$ ) centers [63]. The blue emission is centered at around 491 nm and arises due to structural defects which act as defect donors from Vo and acceptor states from  $\text{Fe}^{3+}$  vacancies in n-type semiconductor metal oxides which can be induced both by the new energy levels in the band gap [62, 64, 65] and by the hole trapped at the metal ion vacancy; it was assigned to the  $\text{F}_2$  center [66, 67]. The orange emission arises at 592 nm due to the relaxation luminescence of defect centers  $\text{F}_2^{1+}$  (or  $\text{V}_{\text{O}}^{+1} + \text{V}_{\text{O}}^0$ ) created because of mechanical stress [63, 66, 67]. The emission may call broader Gaussian fit emissions at 592 nm. The emission band arises in the UV region due to oxygen vacancies (surface defects). The high intense green emission band centered at 521 nm, 535 nm, and 544 nm wavelengths is attributed to oxygen vacancy  $\text{F}(\text{V}_{\text{O}}^0)$  centers. Band gap emission indicates that the hematite nanoparticles have structural defects and rich oxygen vacancies. The oxygen vacancy Vo present at the defect side are good electron scavengers in photocatalytic activity [62]. Peak intensities have been increased with rising calcination temperatures. Owing to the size-associated optical properties in iron oxide nanoparticles, the self-trapped states are observed. The same emission band observed in all the three samples was obtained at different calcination temperatures. The PL optical study has given the physical property of the materials. So, according to the above study,  $\alpha\text{-Fe}_2\text{O}_3$  will be used as a potential material for optoelectronic applications [37].

**3.10. Magnetic Property ( $M-H$  Loop Analysis).** The magnetic hysteresis loop of the hematite nanoparticle  $M-H$  curve under room temperature-dependent field magnetization is shown in Figure 12. The parameters obtained from VSM magnetic saturation ( $M_s$ ), remanent magnetization ( $M_r$ ), and hard coercivity ( $H_c$ ) are tabulated and shown in Table 2. Here, hematite nanoparticles exhibit ferromagnetic behavior at room temperature which was observed from the obtained results and the  $M-H$  curve. The  $M_s$  values of all the three samples obtained at different calcination temperatures are 4.8216, 3.1946, and 0.54164  $\text{emu g}^{-1}$  while comparing bulk iron oxide nanoparticles. These values are low since the  $M_s$  value for bulk iron oxide is 92  $\text{emu g}^{-1}$  [35]. These low  $M_s$ ,  $M_r$ , and  $H_c$  values of hematite nanoparticles clearly indicate that they are in a nanodimension. Hematite nanoparticles are antiferromagnetic in nature since the spins are aligned antiparallel in adjustment planes and parallel in the same plane [37], but here, we report the obtained nanoparticles at different calcination temperatures having an unusual magnetic property owing to surface defects, different crystal structures, nanosizes of the particles, shapes, single domains, and surface charges [36, 38, 68, 69]. Bulk iron oxides have a magnetic property owing to the multiple domains present there. Each domain has spins aligned in the field direction, and uniform magnetization could be separated by each domain wall. Nanodimension iron oxides have a single domain, and the spins are aligned in the same direction with the applied field direction; hence, the coercivity value has been increased [37]. Unusual ferromagnetic behavior is observed in all three samples because of the uncompensated magnetic spin of

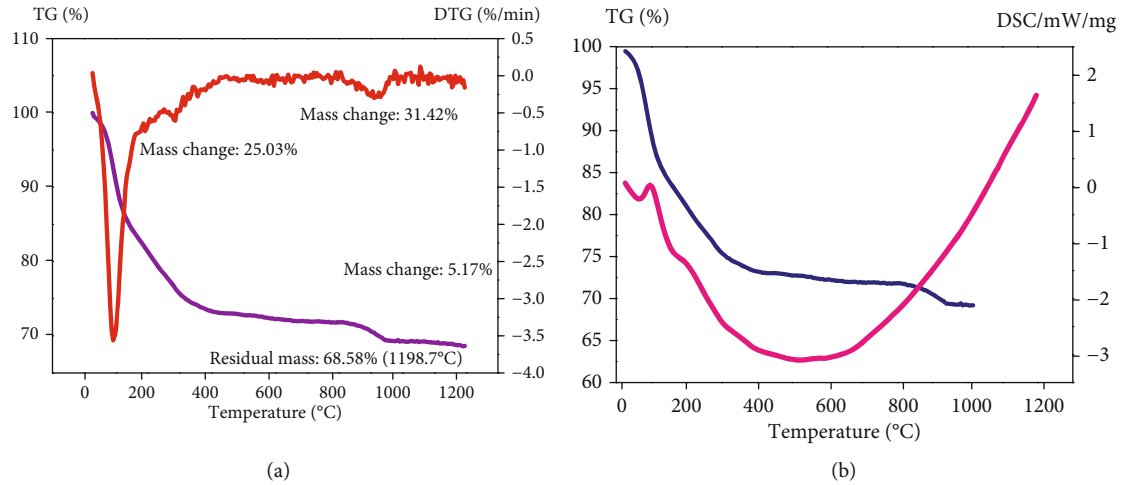


FIGURE 10: TGA/DTA (a) TG-DSC (b) thermograph of hematite nanoparticles.

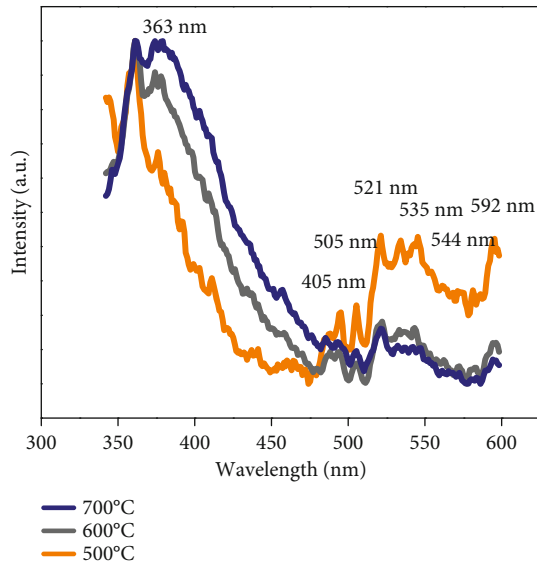


FIGURE 11: Photoluminescence emission spectra of hematite nanoparticles.

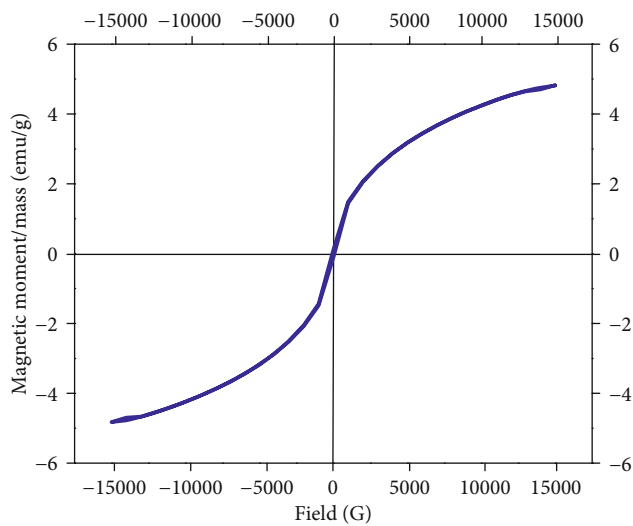
$\text{Fe}^{3+}$  cations [37, 38]. Here, spin order coupling takes place in between the two adjacent planes; it could be called canting spin structure [37]. The sample obtained at a 700°C calcination temperature has an  $H_c$  value of 2761.0 Oe, which is high when compared to the other two sample  $H_c$  values obtained at 600 and 500°C calcination temperatures, and it has not reached saturation due to parasitic magnetism where the electron spin was not rigid at an antiparallel arrangement [70]. The three samples were showing the same RTFM behavior. The  $M_s$  value has decreased while the temperature increased because of the increasing trend of crystallite size [68]. Increasing calcination temperature has created the point defects of oxygen vacancies since oxygen vacancies are close to the surface. So, a point defect has been induced at the surface since it created more oxygen vacancies. It might be one of the reasons for the ferromagnetic nature of hematite nanoparticles [68, 69]. Antiferromagnetic behavior can be destroyed by point defects, so RTFM arises owing to

$\text{Fe}^{3+}\text{-O}^{2-}\text{-Fe}^{3+}$  interactions and yields the uncompensated spins [69]. Here, we have observed that the hematite nanodisc obtained at 700°C has a wide loop hysteresis curve with enhanced coercivity which indicates strong ferromagnetic behavior in a hematite nanodisc. A high coercivity value has been achieved because of the anisotropy particle morphologies and subparticle structure present in hematite nanoparticles [71]. The coercivity value increases with respect to temperature due to variations in the crystallite size and the particle size of hematite nanoparticles [72]. The samples are calcined at different temperatures, so the hysteresis curve also seems to be different at various temperatures. At 500°C, weak ferromagnetism is exhibited, as shown in Figures 12(a)–12(c), whereas at 600 and 700°C, room temperature ferromagnetism is exhibited, as shown in Figures 12(c)–12(f). So the hematite nanodisc obtained at 700°C and 600°C could be potential and promising materials for ferromagnets.

### 3.11. Frequency Dependence Electrical Property of Hematite Nanoparticles

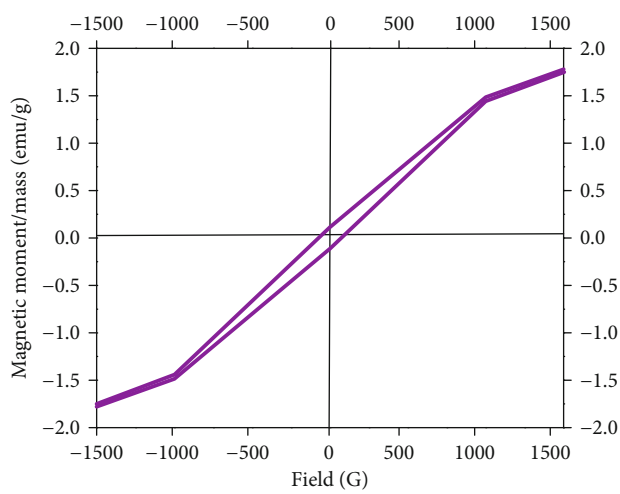
**3.11.1. Real Part of Dielectric Constant ( $\epsilon'$ ).** The hematite nanoparticles are pelletized by hydraulic pressure and coated with silver paste on the surface to create better conduction. Frequency dependence of dielectric properties was studied with varying temperatures from RT to 180°C (30°C, 80°C, 130°C, and 180°C). To design an energy storage device, the dielectric constant and dielectric breakdown strength are the important parameters for calculating the energy density of the dielectrics. Dielectric loss is an important parameter for capacitor performance. The capacitance loss factor is measured by the parallel plate capacitor method using an LCR meter for the frequency range between 100 Hz and 5 MHz with different temperatures (30°C, 80°C, 130°C, and 180°C). The dielectric constant is calculated using the following:

$$\epsilon_r = \frac{C_p \times t}{\epsilon_0 \times A}, \quad (7)$$



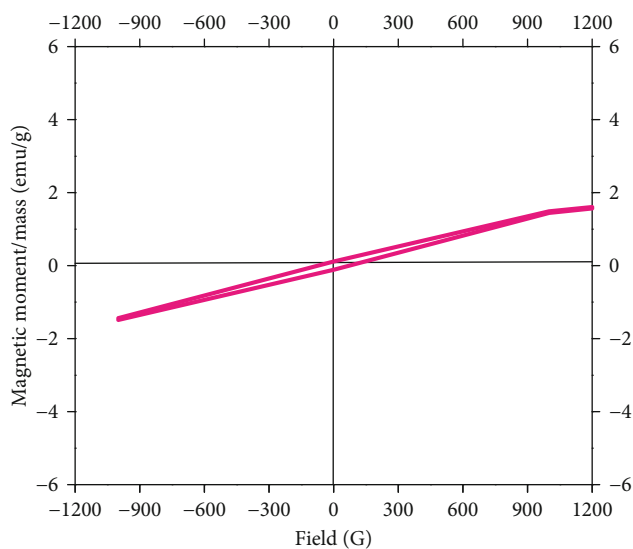
— Fe<sub>2</sub>O<sub>3</sub> 500°C

(a)



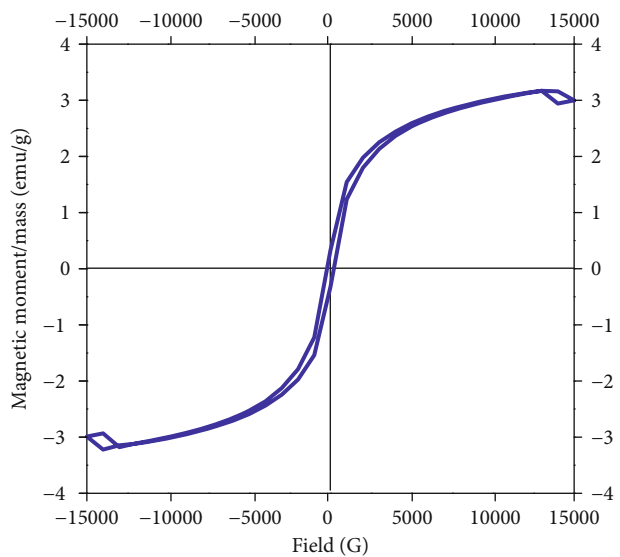
— Fe<sub>2</sub>O<sub>3</sub> 500°C

(b)



— Fe<sub>2</sub>O<sub>3</sub> 500°C

(c)



— Fe<sub>2</sub>O<sub>3</sub> 600°C

(d)

FIGURE 12: Continued.

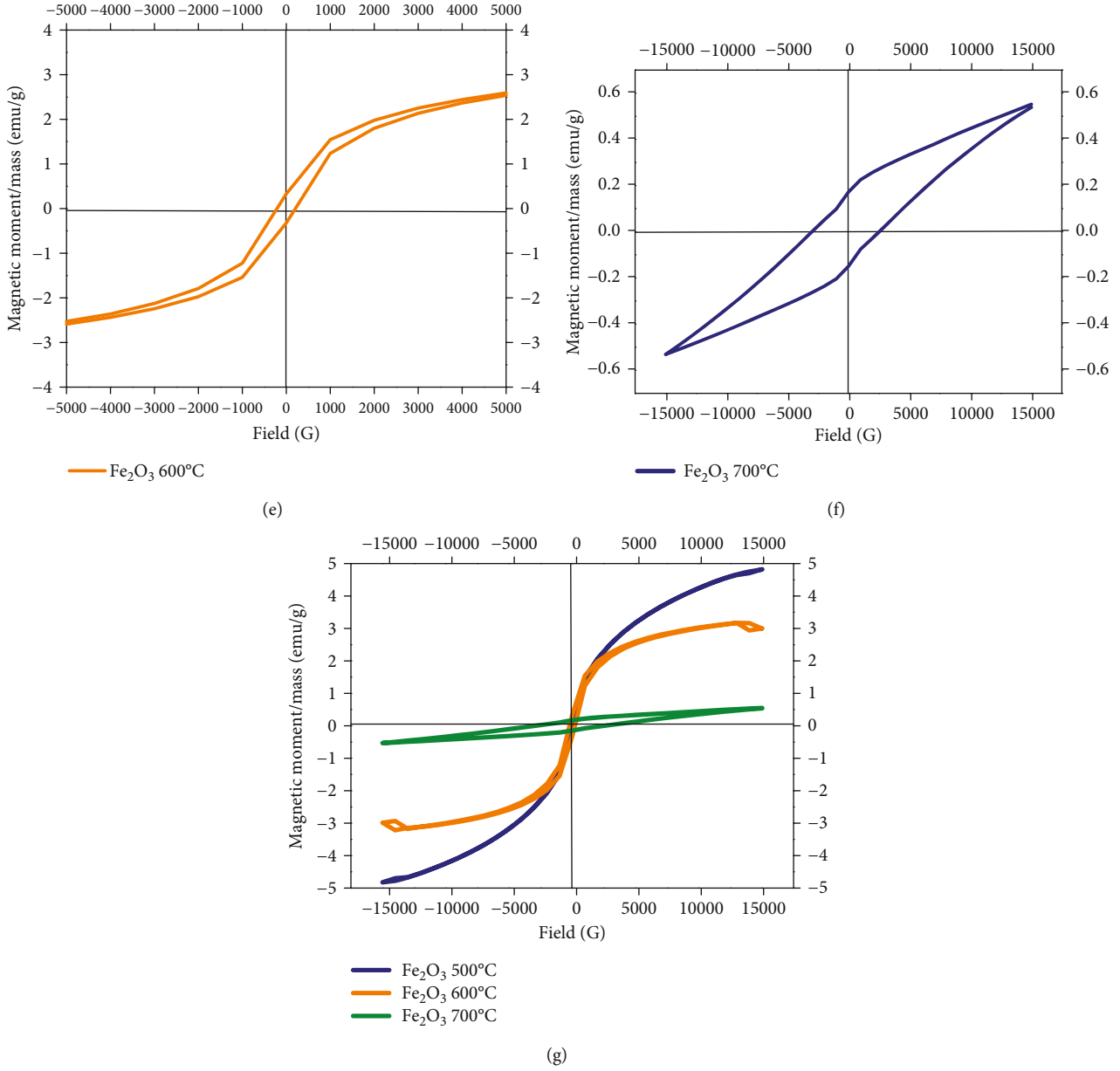


FIGURE 12:  $M$ - $H$  curve (hysteresis loop) of hematite nanoparticles at the room temperature.

TABLE 2: Magnetic parameters from the  $M$ - $H$  (hysteresis loop) curve.

Calcination temperature(°C)	Magnetic saturation (emu/g) (Ms)	Magnetic remanence (emu/g) (Mr)	Magnetic coercivity (Oe) (Hc)
500	4.8216	0.11358	73.022
600	3.1946	0.32480	208.90
700	0.54164	0.16078	2761.0

where  $\epsilon_0$  is the permittivity of the free space ( $8.85 \times 10^{-12}$  Farad per meter (F/m)),  $C_p$  is the capacitance in Farad,  $A$  is the area of the cross-section of the pellet, and  $t$  is the thickness of the pellet.

The five types of polarization, namely, space, charge, dipolar, ionic, and electronic are the reasons for the dielectric nature of materials. When frequency is applied from 100 Hz

to 5 MHz, the dielectric constant increases rapidly along with an increase in frequency due to space charge polarization and interfacial polarization along with temperature increases from RT, as shown in Figures 13(a)–13(c). When the applied frequency increases, the dielectric constant value gradually decreases, while at high-frequency range, its value is a constant along with different temperatures. The same trend has

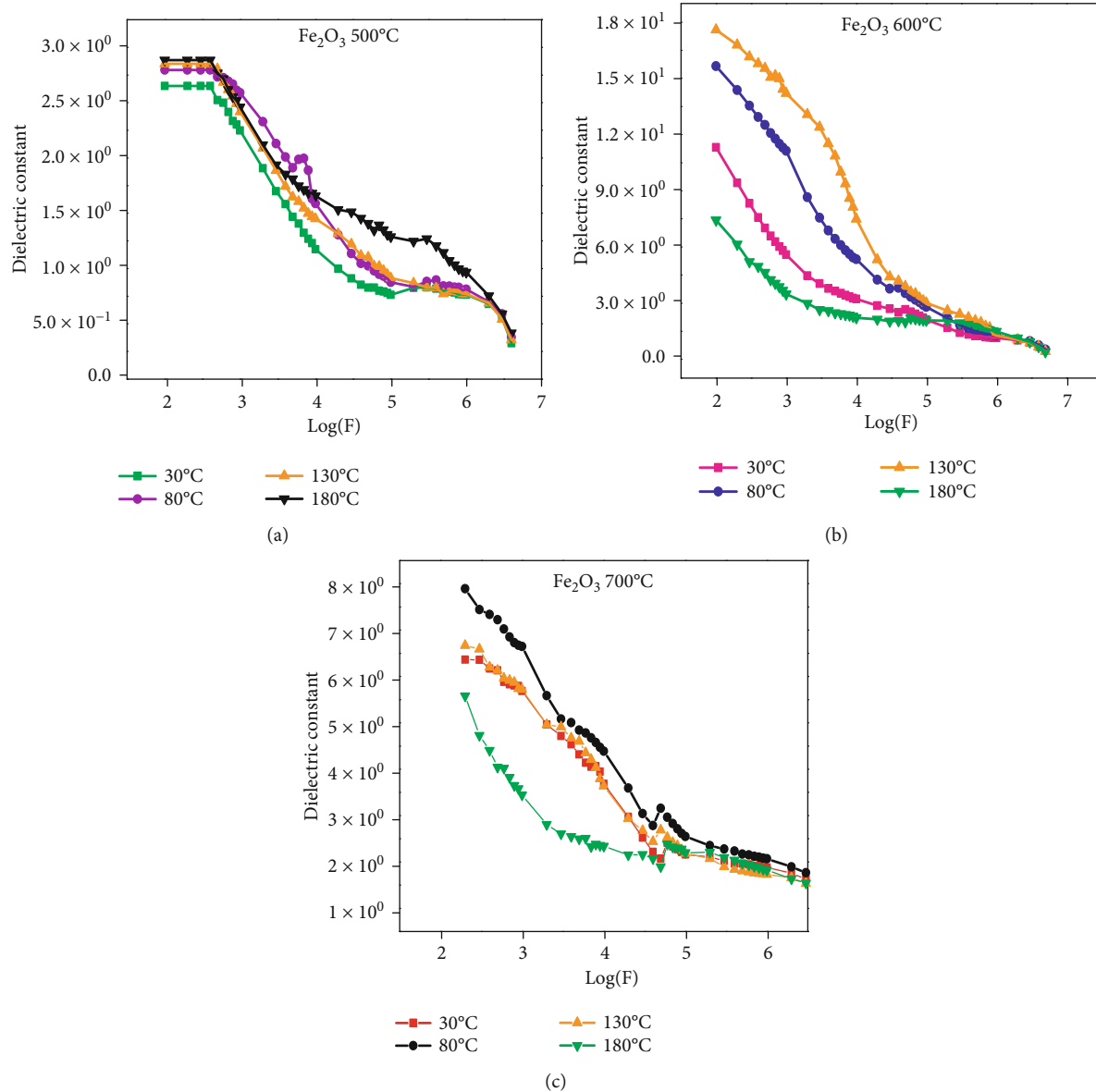


FIGURE 13: Dielectric constant of hematite nanoparticles with different temperatures.

happened by obeying Koop's theory owing to the Maxwell-Wagner-type interfacial polarization. At the high-frequency range, the dielectric constant is found constant and merges due to a decrease in polarization and vacancy defects [71].

**3.11.2. Imaginary Part of Dielectric Constant ( $\epsilon''$ ).** The tan loss decreased with an increase in frequency for all the temperature conditions due to the thermally activated accumulation of charge carriers and space charge polarization. The imaginary part of the dielectric constant value is large at the low-frequency range, as shown in Figures 14(a)–14(c). The polarization mechanism, defects, and thermally activated mobile ion conduction are the reasons for the fast-rising trend of the imaginary part of the dielectric constant at lower frequencies with the thermally activated conduction of mobile ions [72].

**3.11.3. Tan Loss.** The tan loss is high at low frequency but low at high frequency due to the constant reach of the surface polarization value, and therefore, it limits the electrons to follow the AC signals. This is the reason for the high value at low frequency, which disappeared while applying high frequency. The tan loss is shown in Figures 15(a)–15(c). During moderate and low frequencies, the polarization is high, whereas at high frequencies, charges could not follow the AC signals [72]. Due to the domination of the conducting grains, the resistivity comes down, so the loss rises and saturates at a high frequency and it obeys Koop's law. The tan loss is given by the following empirical relation:

$$\text{Tan loss} = \frac{\epsilon'}{\epsilon''}. \quad (8)$$

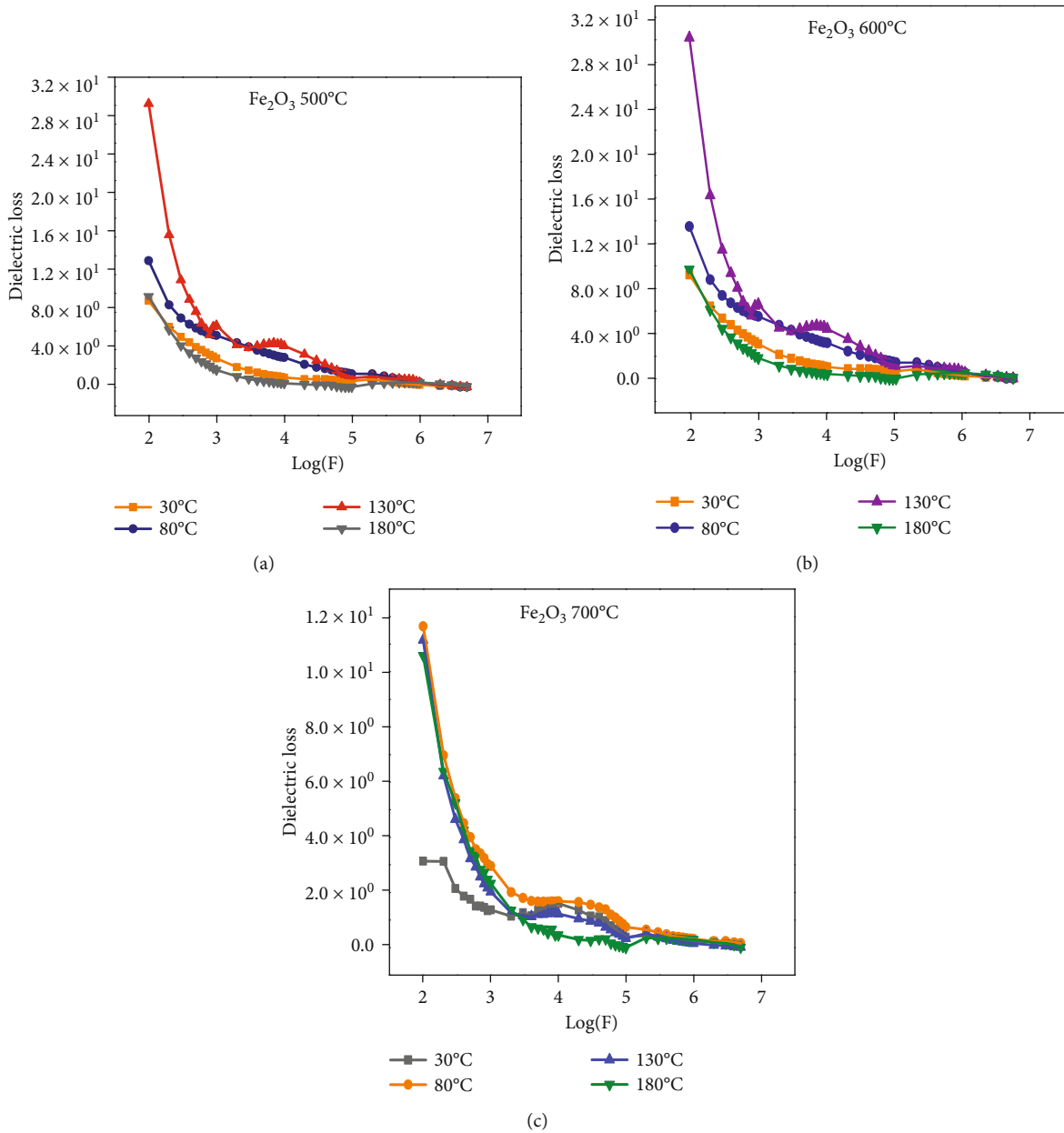


FIGURE 14: Dielectric loss of hematite nanoparticles with different temperatures.

**3.11.4. AC Conductivity Studies.** The frequency-dependent AC conductivity of the iron oxides studied and the graph plotted between frequency and conductivity are shown in Figures 16(a)–16(c). The AC conductivity is at a maximum at higher temperature with high frequency for all the samples due to the presence of a charge carrier and an increase in hopping electrons [73]. Moreover, it obeys the Maxwell-Wagner two-layer model; according to this theory, the conductivity increases gradually along with the frequency [74]. Due to polarization effects at the electrode and electrolyte interface at low frequency, the variation of conductivity occurs. All the values have merged at lower frequency because the grains and grain boundaries are more active; at

low temperature, less charge carriers are available, and there are less hopping electrons, which are the reasons for low conduction at low frequency [73, 75]. AC conductivity is calculated using the following:

$$\sigma = 2\pi f \epsilon \epsilon_0 \tan \delta, \quad (9)$$

where  $\epsilon_0$  is the permittivity of free space ( $8.854 \times 10^{-12}$  F/m).

**3.11.5. Impedance Analysis ( $Z'$  and  $Z''$ ).** Complex impedance ( $Z^* = Z' + iZ''$ ) was analyzed at different temperatures on both sides of the relaxation peak. The frequency and temperature dependence of the real part of impedance ( $Z'$ )

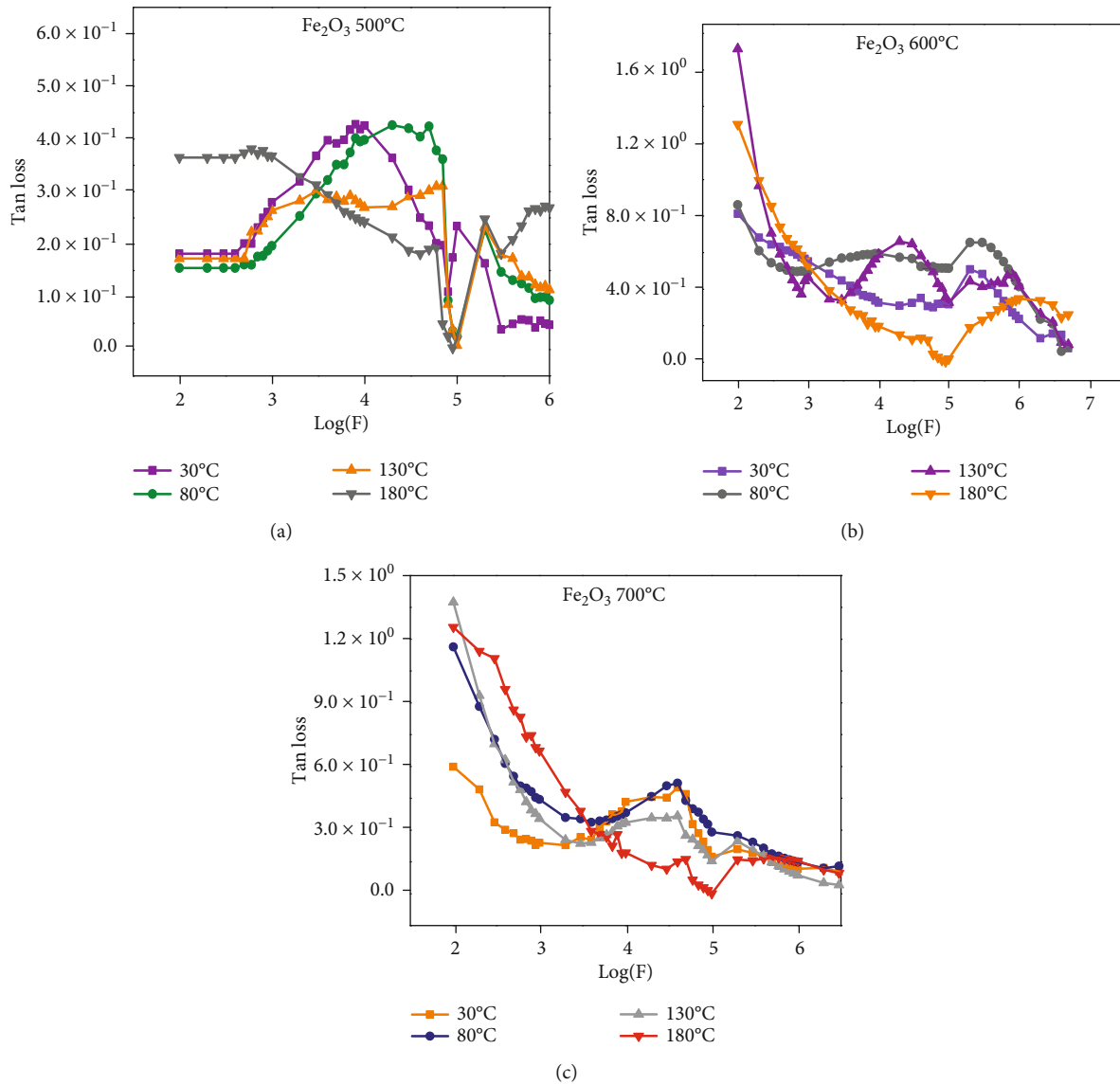


FIGURE 15: Tan loss of hematite nanoparticles with different temperatures.

and the imaginary part of impedance were studied using the following:

$$\begin{aligned} Z' &= \frac{g}{Cp^2\omega^2 + G}, \\ Z'' &= \frac{Cp\omega}{Cp^2\omega^2 + G}, \end{aligned} \quad (10)$$

where  $\omega$  is  $2\pi f$ ,  $G$  is conductance,  $Cp$  is the static capacitance of materials.

**3.11.6. Real Part of Impedance ( $Z'$ ).** The increasing trend of frequency and temperature would decrease the real part of the impedance value owing to a space charge effect, and the values are saturated at high frequency as shown in the figure which is given in the supplementary information and in Figures 17(a), 17(c), and 17(e) where there is an increase in

the conductivity with respect to frequency. At high frequency, the part of the impedance value has merged due to the release of the space charge because of the reduction of the barrier properties or the accumulation of charges at the electrode surface along with the rise of the temperature [76, 77]. A decreasing trend of the  $Z'$  value at high frequency is almost low in all the samples.

Oxygen vacancies in the metal oxides and relaxation process in the materials are the reasons why the frequency-dependent imaginary part of impedance shifted to a higher frequency with an increase in temperature. At higher temperature, the values are saturated and merged at higher frequency [76, 77], as shown in the supplementary information and in Figures 17(b), 17(d), and 17(f).

**3.11.7. Cole-Cole Plot or Nyquist Plot.** The graph plotted between the real part of impedance ( $Z'$ ) and the imaginary

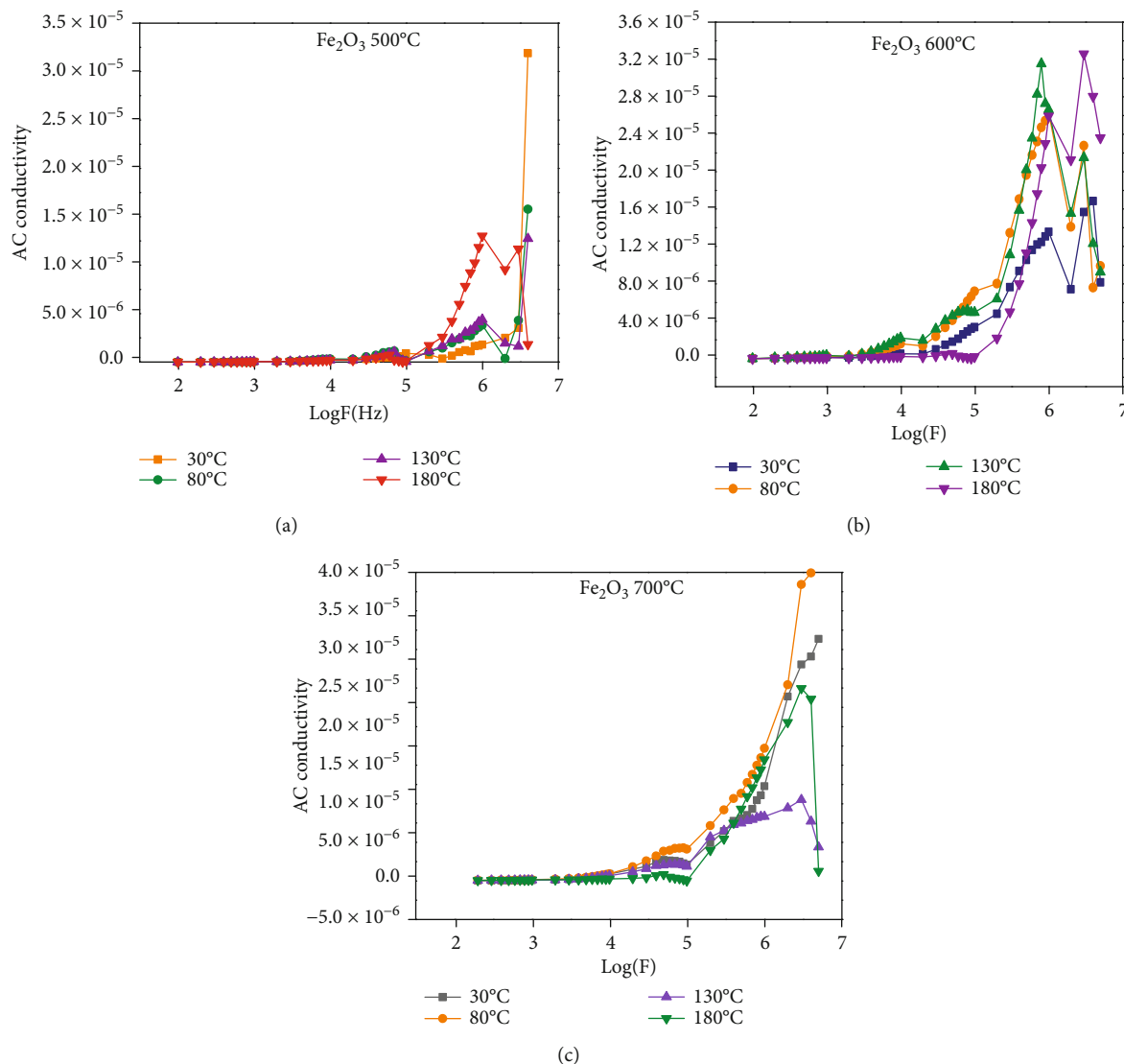


FIGURE 16: AC conductivity of hematite nanoparticles with different temperatures.

parts of impedance ( $Z''$ ) are shown in Figures 18(a)–18(c). From Figure 18, the semicircle with distinct radii appears at low frequency due to grain boundaries [75–77]. The semicircle decreases with increasing temperature due to the negative temperature coefficient of materials which are promising materials for thermistor applications.

### 3.12. Visible-Light-Driven Photodegradation of Methylene Blue Dye by Hematite Nanodisc

**3.12.1. Photocatalytic Analysis of  $\text{Fe}_2\text{O}_3$  NPs.** The key factors to determine the photocatalytic activity of the hematite nanoparticles are atomic structure, surface area, and its electronic structure. The SEM analysis revealed that the synthesized nanoparticles have different morphologies such as nanodiscs, nanoplates, and sheets at 700, 600, and 500 degrees Celsius, and its band gap has been calculated from the DRS spectrum. Its band gap energy is 1.7 eV, 1.5 eV, and 1.2 eV. Here, we

exhibited only hematite nanodisc methylene blue degradation in aqueous medium. The degradation process went on under sunlight since its band gap energy is at the visible region of the electromagnetic spectrum. The reason for picking the nanodisc for degradation is because, based on TG-DSC and XRD reports, a complete hematite structure was formed after 500 degree Celsius. To study the photocatalytic activity, the prepared sample was dispersed in dye solution and kept in the dark for 1 hour to achieve adsorption-desorption equilibrium. The time-dependent UV spectrum of a hematite nanodisc sample is shown in Figure 19(a). The change in concentration with respect to reaction time is shown in Figure 19(b). The main factors that degrade the dye molecules are hydroxyl radicals ( $\cdot\text{OH}$ ), superoxide anions ( $\cdot\text{O}_2^-$ ), and light. When the semiconductor metal oxide sample is exposed to a light source, the free electrons on the surface of the sample will absorb the light photons and are excited from a valance band to a conduction band.

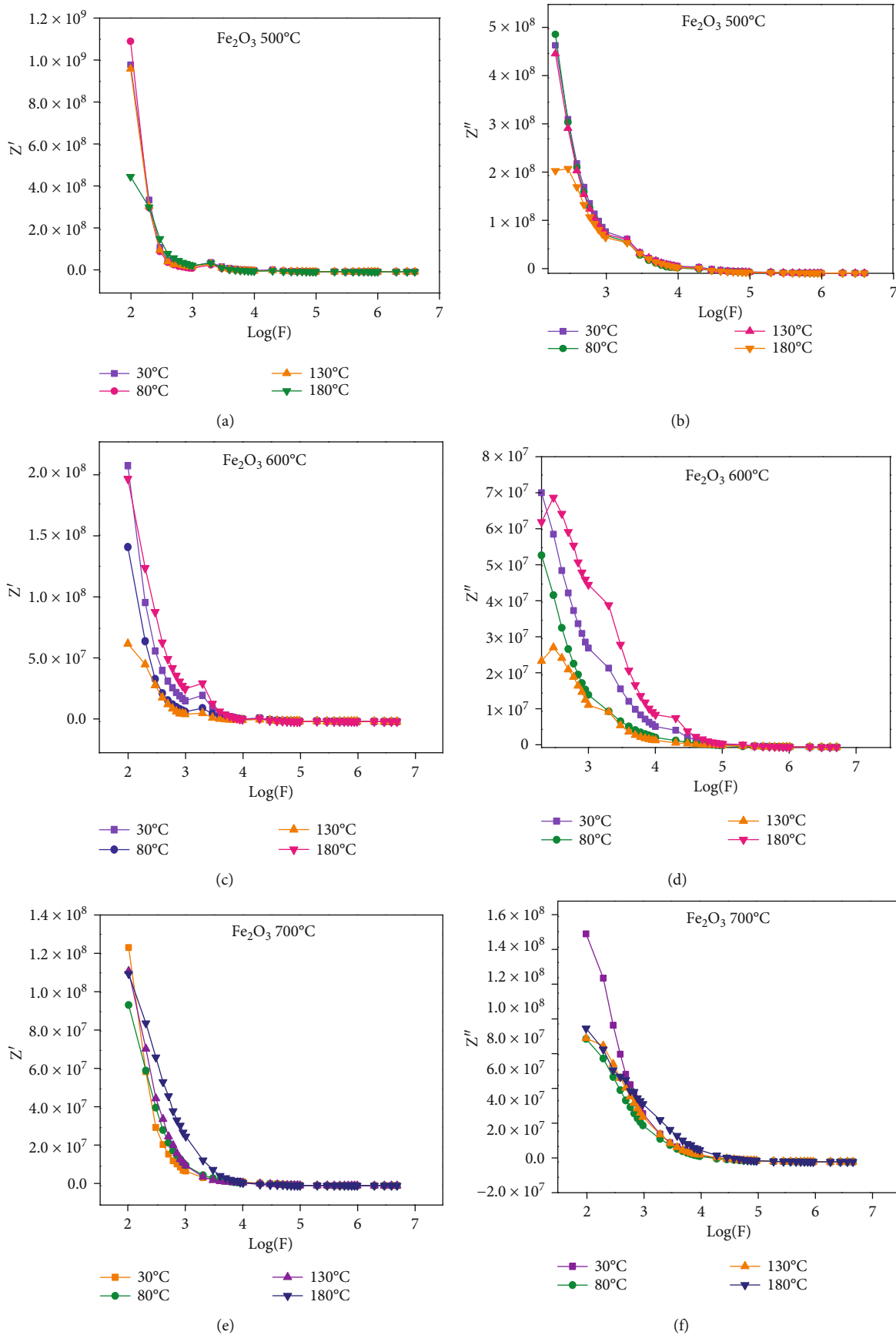


FIGURE 17: Real part and imaginary part of impedance ( $Z'$  and  $Z''$ ) at 500°C (a, b), 600°C (c, d), and 700°C (e, f).

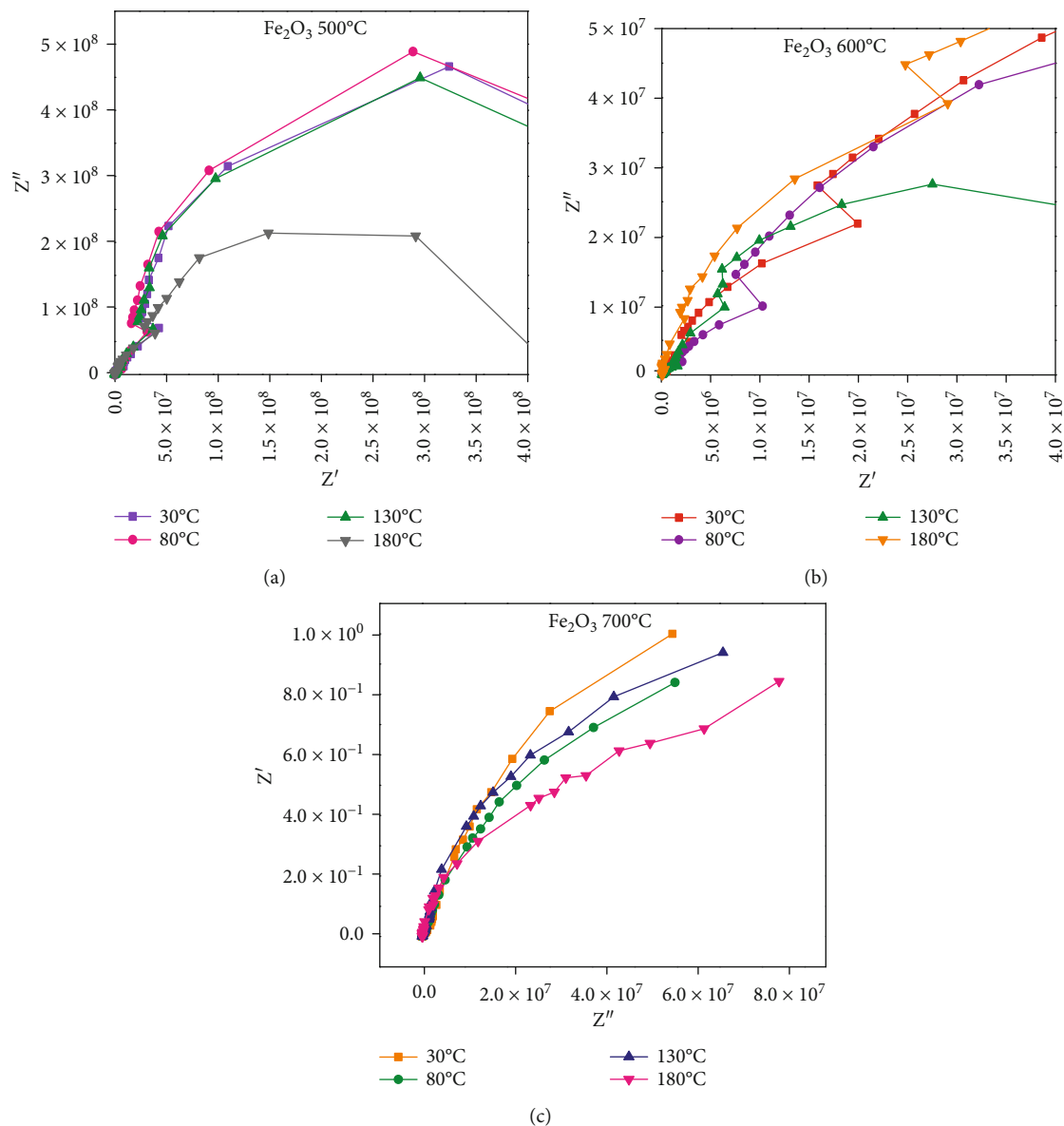


FIGURE 18: Nyquist plot of 500 (a), 600 (b), and 700°C (c).

These excited electrons react with oxygen to produce superoxide anions, and holes react with water to produce hydroxyl radicals. Also, H<sub>2</sub>O<sub>2</sub> was produced as an intermediate product during the reaction; hence, H<sub>2</sub>O<sub>2</sub> absorbs electrons and again produces (<sup>•</sup>OH). Here, one more probability is a Fenton-like process, i.e., the Fe<sup>2+</sup> ion reacts with H<sub>2</sub>O<sub>2</sub> and also produces (<sup>•</sup>OH). Hence, these (<sup>•</sup>OH) radicals and (<sup>•</sup>O<sup>2-</sup>) play a vital role in the degradation of dye molecules. For a comparative study, all the three prepared samples were subjected to photocatalysis, but the sample prepared at 500 and 600 degrees Celsius did not have much impact on degradation; there is only very small degradation that occurred since the complete hematite structure was formed after 500 degrees Celsius indicating the amorphous and low degree of crystalline nature of the sample. However, the hematite nanodisc which was obtained at 700 degrees Celsius shows better

results in the degradation process owing to its crystalline nature, which means that the cations are regularly arranged on the surface of the sample. From the PL spectrum, it is evident that the hematite nanoparticle has high defects like oxygen vacancies, so it provides more active sites for the degradation process. On the other hand, the band gap is slightly smaller compared to the other two samples. This may delay the electron-hole recombination rate, which is also a key factor for degradation. So the hematite nanodisc degrades up to 69% of the dye molecules within 2 hours of visible-light irradiation.

The quantitative analysis of the reaction kinetics of the sample in the degradation performance of MB was calculated using the Langmuir–Hinshelwood equation. This model narrates the chemical kinetics of the reaction for the photodegradation of dye molecules, and it is shown in Figure 19(c). To

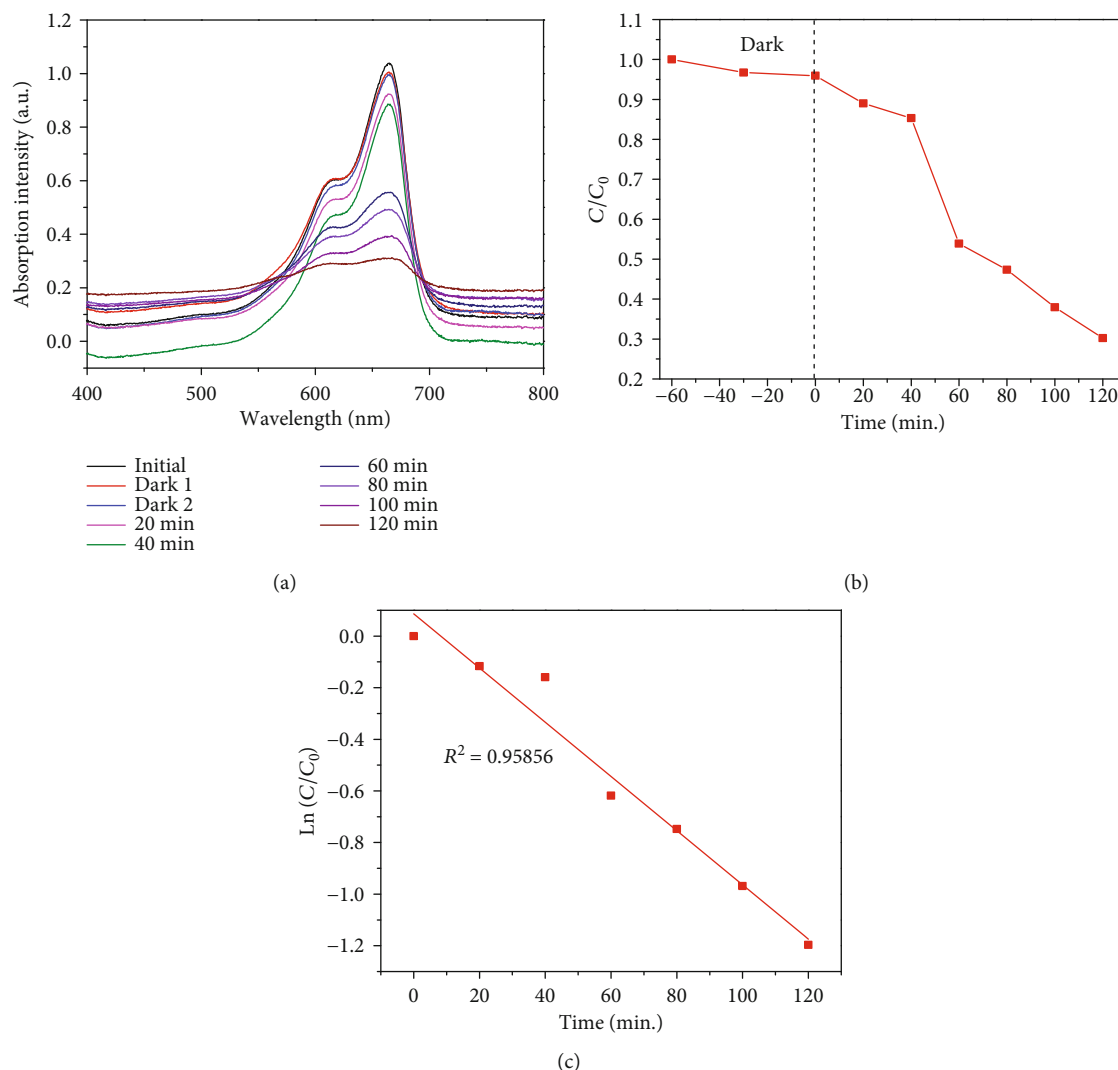


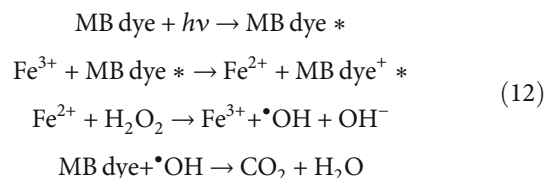
FIGURE 19: Photodegradation of methylene blue dye UV-vis absorbance spectra.

calculate the rate constant and the  $R^2$  value, a linear fit for the graph between  $\ln(C/C_0)$  and irradiation time was drawn and obtained from the slope value. The degradation reaction follows the pseudo-first-order kinetics. The rate constant gives information about the approximate number of dye molecules dissociated per second during the photodegradation process:

$$\ln(C/C_0) = kt, \quad (11)$$

where  $C$  is the change in the concentration of a dye;  $C_0$  is the initial concentration of the dye solution, the solution with respect to time; and  $k$  is the first-order rate constant. The rate constant and  $R^2$  value of the reaction was found to be  $10.51 \times 10^{-3} \text{ s}^{-1}$  and 0.95856.

**3.12.2. Degradation Mechanism of MB Dye by  $\text{Fe}^{3+}$  Ions.** The surface density of  $\text{Fe}^{3+}$  ions is high, so it degraded the dye easily:



Here, any additives that have  $\text{H}_2\text{O}_2$  were not added into the degradation process. We used only a magnetic photocatalyst alone throughout the process of degradation. The degradation mechanism is shown above where additives are produced by the reaction itself as an intermediate product. The hematite nanodisc obtained by this green synthesis protocol can be used as a magnetically separate able nanocatalyst. This is a low-cost, simple, biodegradable, most stable, nontoxic magnetic visible-light photocatalyst.

## 4. Conclusion

Here, we have prepared surfactant-free, nontoxic, highly stable, pure  $\alpha\text{-Fe}_2\text{O}_3$  nanoparticles by a simple, rapid, one-step

phytochemical-assisted method where the bioactive compounds play an important role in the formation of magnetic nanoparticles and they act as stabilizing and capping agents. The prepared hematite nanoparticles have a single phase with a rhombohedral crystal structure; an R-3c space group was confirmed by PXRD, and the calculated crystallite size was 23 nm and 35 nm at 600 and 700 degrees Celsius annealing temperature. Surface plasmon resonance was blue shifted with rising calcination temperature at the visible region with a narrow band gap, and the calculated  $E_g$  values were 1.7 eV, 1.5 eV, and 1.2 eV at 500, 600, and 700 degrees Celsius. It exhibited multicolor photoluminescence from a near UV emission band to the orange visible region, and the emission bands in the visible region were due to surface defects and the oxygen vacancy  $V_o$ . The SEM micrographs illustrated that the nanoparticles have different morphologies with different annealing temperatures due to surface energy. All the synthesized samples were in nanoscale with a polycrystalline nature and conformed with TEM analysis with the SAED pattern. VSM measurements exhibited narrow and wide hysteresis loops with weak and strong magnetic behavior in nature at room temperature due to the surface density and defects and oxygen vacancies, crystallite size, particle size, and shape anisotropy. The hematite nanodisc achieved a high coercivity value (2761 Oe) and has strong room temperature ferromagnetism since it has a single domain and anisotropy, size, crystal structure particle morphologies, and subparticle structure present in the iron nanoparticles. FTIR spectrum has revealed the role of bioactive molecules in a nanoparticle formation. Thermal analysis has given the information about weight loss and decomposition of water and organic wastes and phase transformation regarding hematite nanoparticles. Dielectric constant and dielectric loss and AC conductivity behavior have increased with increasing temperature owing to the electron hopping mechanism. It has a semiconductor behavior since the resistance value is decreased and the AC value increased with rising temperature. Dielectric dispersion and the AC value have changed with frequency due to the space charge and interfacial polarization. This was explained using the Maxwell-Wagner model. Complex impedance analysis and the AC conductivity of samples are rising trends with increasing frequency due to a grain-resistant better match with the CBH (Correlated Barrier Hopping) model. The Nyquist plot exhibits a non-Debye relaxation type. Hematite nanoparticles have high photocatalytic activity under an electromagnetic spectrum owing to a narrow band gap, with the surface plasmon resonance at the visible region. The prepared magnetic visible-light photocatalyst degraded the methylene blue dye in an aqueous medium efficiently without the addition of any additives. In addition to this, it could be a potential candidate in water splitting and removing organic pollutants, spintronics, and ferromagnet storage devices.

### Data Availability

All the data analyzed or used during this study are included within this article.

### Conflicts of Interest

The authors declare that they have no conflicts of interest.

### Acknowledgment

The authors thank to the University College of Engineering-Anna University-Regional Campus, Trichy, for providing stipends under TEQUIP-II. The authors would like to show their gratitude to Dr. S. Kalainathan, Senior Professor, Centre for Nanotechnology Research, VIT, Vellore, Tamil Nadu, India, for his valuable guidance during the course of their research, particularly in dielectric studies and TEM studies. The authors are also immensely grateful to Dr. Venu Reddy, HOD, Department of Chemistry and Nanotechnology Research Centre, SRKR Engineering College, Bhimavaram 534204, Andhra Pradesh, India, for his timely help. The authors also sincerely thank Dr. K. Nehru, Associate Professor, Department of Chemistry, Anna University, Trichy, and Dr. Arul Mozhi, Associate Professor and Head, Petrochemical Technology, Anna University, Trichy, for their kind cooperation during our lab work.

### References

- [1] S. Baker, D. Rakshith, K. S. Kavitha et al., "Plants: emerging as nanofactories towards facile route in synthesis of nanoparticles," *BioImpacts*, vol. 3, no. 3, p. 111, 2013.
- [2] P. Kuppusamy, M. M. Yusoff, G. P. Maniam, and N. Govindan, "Biosynthesis of metallic nanoparticles using plant derivatives and their new avenues in pharmacological applications - An updated report," *Saudi Pharmaceutical Journal*, vol. 24, no. 4, pp. 473-484, 2016.
- [3] A. K. Mittal, Y. Chisti, and U. C. Banerjee, "Synthesis of metallic nanoparticles using plant extracts," *Biotechnology Advances Biotechnol*, vol. 31, no. 2, pp. 346-356, 2013.
- [4] S. Li, Y. Shen, A. Xie et al., "Green synthesis of silver nanoparticles using *Capsicum annum L.* extract," *Green Chemistry*, vol. 9, no. 8, pp. 852-858, 2007.
- [5] D. Mandal, M. E. Bolander, D. Mukhopadhyay, G. Sarkar, and P. Mukherjee, "The use of microorganisms for the formation of metal nanoparticles and their application," *Applied Microbiology and Biotechnology*, vol. 69, no. 5, pp. 485-492, 2006.
- [6] D. Cui and H. Gao, "This article has been retracted. Advance and prospect of bionanomaterials," *Biotechnology Progress*, vol. 19, no. 3, pp. 683-692, 2003.
- [7] H. Bar, D. K. Bhui, G. P. Sahoo, P. Sarkar, S. P. de, and A. Misra, "Green synthesis of silver nanoparticles using latex of *Jatropha curcas*," *Colloids and Surfaces A: Physicochemical and Engineering Aspects*, vol. 339, no. 1-3, pp. 134-139, 2009.
- [8] S. S. Shankar, A. Ahmad, R. Pasricha, and M. Sastry, "Bioreduction of chloroaurate ions by geranium leaves and its endophytic fungus yields gold nanoparticles of different shapes," *Journal of Materials Chemistry*, vol. 13, no. 7, pp. 1822-1826, 2003.
- [9] V. Armendariz, I. Herrera, J. R. peralta-vidua et al., "Size controlled gold nanoparticle formation by *Avena sativa* biomass: use of plants in nanobiotechnology," *Journal of Nanoparticle Research*, vol. 6, no. 4, pp. 377-382, 2004.

- [10] V. Armendariz, J. L. Gardea-Torresdey, M. Jose-Yacaman, J. Gonzalez, and I. Herrera, "Gold nanoparticle formation by oat and wheat biomasses," pp. 1-2, 2002.
- [11] I. Herrera, J. L. Gardea-Torresdey, K. J. Tiemann, J. R. Peralta-Videa, V. Armendariz, and J. G. Parsons, "Binding of silver (I) ions by alfalfa biomass (*Medicago sativa*): batch pH, time, temperature, and ionic strength studies," *Journal of Hazardous Substance Research*, vol. 4, no. 1, p. 1, 2003.
- [12] J. L. Gardea-Torresdey, E. Gomez, J. R. Peralta-Videa, J. G. Parsons, H. Troiani, and M. Jose-Yacaman, "Alfalfa sprouts: a natural source for the synthesis of silver nanoparticles," *Langmuir*, vol. 19, no. 4, pp. 1357-1361, 2003.
- [13] J. Huang, Q. Li, D. Sun et al., "Biosynthesis of silver and gold nanoparticles by novel sundried *Cinnamomum camphora* leaf," *Nanotechnology*, vol. 18, no. 10, article 105104, 2007.
- [14] V. Parashar, R. Parashar, B. Sharma, and A. C. Pandey, "Parthenium leaf extract mediated synthesis of silver nanoparticles: a novel approach towards weed utilization," *Digest Journal of Nanomaterials & Biostructures*, vol. 4, no. 1, 2009.
- [15] U. K. Parashar, P. S. Saxena, and A. Srivastava, "Bioinspired synthesis of silver nanoparticles," *Digest Journal of Nanomaterials & Biostructures*, vol. 4, no. 1, 2009.
- [16] M. Rai and A. Yadav, "Plants as potential synthesiser of precious metal nanoparticles: progress and prospects," *IET Nanobiotechnology*, vol. 7, no. 3, pp. 117-124, 2013.
- [17] C. Ramachandran, K. V. Peter, and P. K. Gopalakrishnan, "Drumstick (*Moringa oleifera*): a multipurpose Indian vegetable," *Economic Botany*, vol. 34, no. 3, pp. 276-283, 1980.
- [18] M. U. Dahot, "Vitamin contents of the flowers and seeds of *Moringa oleifera*," *Pakistan Journal of Biochemistry*, vol. 21, 1988.
- [19] C. H. Bosch, "*Moringa stenopetala* (Baker f.) Cufod," *PROTA*, vol. 2, pp. 395-397, 2004.
- [20] P. T. Anastas and J. B. Zimmerman, *Why we need a green nano award & how to make it happen*, vol. 1, Woodrow Wilson International Center for Scholars, Washington DC, 2007.
- [21] T. Baran and M. Nasrollahzadeh, "Facile fabrication of magnetically separable palladium nanoparticles supported on modified kaolin as a highly active heterogeneous catalyst for Suzuki coupling reactions," *Journal of Physics and Chemistry of Solids*, vol. 146, article 109566, 2020.
- [22] D.-Y. Zhang, X.-Q. Zhang, X.-H. Yao et al., "Microwave-assisted synthesis of PdNPs by cellulose solution to prepare 3D porous microspheres applied on dyes discoloration," *Carbohydrate Polymers*, vol. 247, article 116569, 2020.
- [23] V. Kumar and S. K. Yadav, "Plant-mediated synthesis of silver and gold nanoparticles and their applications," *Journal of Chemical Technology & Biotechnology*, vol. 84, no. 2, pp. 151-157, 2009.
- [24] K. S. Mukunthan and S. Balaji, "Cashew apple juice (*Anacardium occidentale* L.) speeds up the synthesis of silver nanoparticles," *International Journal of Green Nanotechnology*, vol. 4, no. 2, pp. 71-79, 2012.
- [25] J. Gangwar, B. K. Gupta, and A. K. Srivastava, "Prospects of emerging engineered oxide nanomaterials and their applications," *Defence Science Journal*, vol. 66, no. 4, p. 323, 2016.
- [26] Z. Nie, A. Petukhova, and E. Kumacheva, "Properties and emerging applications of self-assembled structures made from inorganic nanoparticles," *Nature Nanotechnology*, vol. 5, no. 1, pp. 15-25, 2010.
- [27] X. Wang, L. Yu, P. Hu, and F. Yuan, "Synthesis of single-crystalline hollow octahedral NiO," *Crystal Growth and Design*, vol. 7, no. 12, pp. 2415-2418, 2007.
- [28] Z. Chen, Z. Jiao, D. Pan et al., "Recent advances in manganese oxide nanocrystals: fabrication, characterization, and microstructure," *Chemical Reviews*, vol. 112, no. 7, pp. 3833-3855, 2012.
- [29] J. Gangwar, K. K. Dey, P. Komal, S. K. Tripathi, and A. K. Srivastava, "Microstructure, phase formations and optical bands in nanostructured alumina," *Advanced Materials Letters*, vol. 2, no. 6, pp. 402-408, 2011.
- [30] Z. W. Pan, Z. R. Dai, and Z. L. Wang, "Nanobelts of semiconducting oxides," *Science*, vol. 291, no. 5510, pp. 1947-1949, 2001.
- [31] P. M. Valencia, O. C. Farokhzad, R. Karnik, and R. Langer, "Microfluidic technologies for accelerating the clinical translation of nanoparticles," *Nature Nanotechnology*, vol. 7, no. 10, pp. 623-629, 2012.
- [32] J. Gangwar, A. K. Srivastava, S. K. Tripathi, M. Wan, and R. R. Yadav, "Strong enhancement in thermal conductivity of ethylene glycol-based nanofluids by amorphous and crystalline Al<sub>2</sub>O<sub>3</sub> nanoparticles," *Applied Physics Letters*, vol. 105, no. 6, article 063108, 2014.
- [33] S. Shang, K. Xue, D. Chen, and X. Jiao, "Preparation and characterization of rose-like NiO nanostructures," *CrystEngComm*, vol. 13, no. 16, pp. 5094-5099, 2011.
- [34] G. Zelmanov and R. Semiat, "Iron(3) oxide-based nanoparticles as catalysts in advanced organic aqueous oxidation," *Water Research*, vol. 42, no. 1-2, pp. 492-498, 2008.
- [35] W. Wu, C. Z. Jiang, and V. A. L. Roy, "Designed synthesis and surface engineering strategies of magnetic iron oxide nanoparticles for biomedical applications," *Nanoscale*, vol. 8, no. 47, pp. 19421-19474, 2016.
- [36] Y. Zong, Y. Sun, S. Meng et al., "Doping effect and oxygen defects boost room temperature ferromagnetism of Co-doped ZnO nanoparticles: experimental and theoretical studies," *RSC Advances*, vol. 9, no. 40, pp. 23012-23020, 2019.
- [37] S. Riaz, S. Z. H. Shah, Z. N. Kayani, and S. Naseem, "Magnetic and structural phase transition in iron oxide nanostructures," *Materials Today: Proceedings*, vol. 2, no. 10, pp. 5280-5287, 2015.
- [38] F. N. Sayed and V. Polshettiwar, "Facile and sustainable synthesis of shaped iron oxide nanoparticles: effect of iron precursor salts on the shapes of iron oxides," *Scientific Reports*, vol. 5, no. 1, pp. 1-14, 2015.
- [39] X. Zhou, H. Yang, C. Wang et al., "Visible light induced photocatalytic degradation of rhodamine B on one-dimensional iron oxide particles," *The Journal of Physical Chemistry C*, vol. 114, no. 40, pp. 17051-17061, 2010.
- [40] T. Baran and I. Sargin, "Green synthesis of a palladium nanocatalyst anchored on magnetic lignin-chitosan beads for synthesis of biaryls and aryl halide cyanation," *International Journal of Biological Macromolecules*, vol. 155, pp. 814-822, 2020.
- [41] T. Baran and M. Nasrollahzadeh, "Facile synthesis of palladium nanoparticles immobilized on magnetic biodegradable microcapsules used as effective and recyclable catalyst in Suzuki-Miyaura reaction and p-nitrophenol reduction," *Carbohydrate Polymers*, vol. 222, article 115029, 2019.
- [42] M. Nasrollahzadeh, N. Motahharifar, F. Ghorbannezhad, N. S. Bidgoli, T. Baran, and R. S. Varma, "Recent advances in

- polymer supported palladium complexes as (nano) catalysts for Sonogashira coupling reaction,” *Molecular Catalysis*, vol. 480, article 110645, 2020.
- [43] J. Torrent and V. Barrón, “Diffuse reflectance spectroscopy of iron oxides,” *Encyclopedia of Surface and Colloid Science*, vol. 1, pp. 1438–1446, 2002.
- [44] D. A. Wheeler, G. Wang, Y. Ling, Y. Li, and J. Z. Zhang, “Nanostructured hematite: synthesis, characterization, charge carrier dynamics, and photoelectrochemical properties,” *Energy & Environmental Science*, vol. 5, no. 5, pp. 6682–6702, 2012.
- [45] I. Muneer, M. A. Farrukh, and R. Raza, “Influence of annealing temperature on the physical and photoelectric properties of Gd/Fe<sub>1.727</sub>Sn<sub>0.205</sub>O<sub>3</sub> nanoparticles for solid oxides fuel cell application,” *Journal of Sol-Gel Science and Technology*, vol. 94, no. 1, pp. 98–108, 2020.
- [46] A. S. Keiteb, E. Saion, A. Zakaria, and N. Soltani, “Structural and optical properties of zirconia nanoparticles by thermal treatment synthesis,” *Journal of Nanomaterials*, vol. 2016, 6 pages, 2016.
- [47] N. Badar, N. F. Chayed, R. Roshidah, N. Kamarudin, and N. Kamarulzaman, “Band gap energies of magnesium oxide nanomaterials synthesized by the sol-gel method,” *Advanced Materials Research*, vol. 545, pp. 157–160, 2012.
- [48] H. Y. Zahran, S. S. Shneouda, I. S. Yahia, and F. El-Tantawy, “Facile and rapid synthesis of nanoplates Mg(OH)<sub>2</sub> and MgO via microwave technique from metal source: structural, optical and dielectric properties,” *Journal of Sol-Gel Science and Technology*, vol. 86, no. 1, pp. 104–111, 2018.
- [49] L. Madianos, G. Tsekenis, E. Skotadis, L. Patsiouras, and D. Tsoukalas, “A highly sensitive impedimetric aptasensor for the selective detection of acetamiprid and atrazine based on microwires formed by platinum nanoparticles,” *Biosensors and Bioelectronics*, vol. 101, pp. 268–274, 2018.
- [50] T. Adinaveen, J. Judith Vijaya, and L. John Kennedy, “Studies on the structural, morphological, optical, and magnetic properties of  $\alpha$ -Fe<sub>2</sub>O<sub>3</sub> nanostructures by a simple one-step low temperature reflux condensing method,” *Journal of Superconductivity and Novel Magnetism*, vol. 27, no. 7, pp. 1721–1727, 2014.
- [51] Y. Zheng, L. Cao, G. Xing, Z. Bai, J. Huang, and Z. Zhang, “Microscale flower-like magnesium oxide for highly efficient photocatalytic degradation of organic dyes in aqueous solution,” *RSC Advances*, vol. 9, no. 13, pp. 7338–7348, 2019.
- [52] A. Arulraj, S. Govindan, S. Vadivel, and B. Subramanian, “Photovoltaic performance of TiO<sub>2</sub> using natural sensitizer extracted from *Phyllanthus reticulatus*,” *Journal of Materials Science: Materials in Electronics*, vol. 28, no. 24, pp. 18455–18462, 2017.
- [53] J. A. Morales-Morales, “Synthesis of hematite  $\alpha$ -Fe<sub>2</sub>O<sub>3</sub> nano powders by the controlled precipitation method,” *Ciencia en Desarrollo*, vol. 8, no. 1, pp. 99–107, 2017.
- [54] S. F. Bdewi, O. G. Abdullah, B. K. Aziz, and A. A. R. Mutar, “Synthesis, structural and optical characterization of MgO nanocrystalline embedded in PVA matrix,” *Journal of Inorganic and Organometallic Polymers and Materials*, vol. 26, no. 2, pp. 326–334, 2016.
- [55] J. Jeevanandam, Y. S. Chan, and Y. H. Ku, “Aqueous *Eucalyptus globulus* leaf extract-mediated biosynthesis of MgO nanorods,” *Applied Biological Chemistry*, vol. 61, no. 2, pp. 197–208, 2018.
- [56] N. Sethy, Z. Arif, P. K. Mishra, and P. Kumar, “Green synthesis of TiO<sub>2</sub> nanoparticles from *Syzygium cumini* extract for photo-catalytic removal of lead (Pb) in explosive industrial wastewater,” *Green Processing and Synthesis*, vol. 9, no. 1, pp. 171–181, 2020.
- [57] P. N. V. K. Pallela, S. Ummey, L. K. Ruddaraju et al., “Antibacterial efficacy of green synthesized  $\alpha$ -Fe<sub>2</sub>O<sub>3</sub> nanoparticles using *Sida cordifolia* plant extract,” *Heliyon*, vol. 5, no. 11, article e02765, 2019.
- [58] M. A. Vargas, J. E. Diosa, and E. Mosquera, “Data on study of hematite nanoparticles obtained from Iron(III) oxide by the Pechini method,” *Data in Brief*, vol. 25, article 104183, 2019.
- [59] Z. N. Kayani, S. Arshad, S. Riaz, and S. Naseem, “Synthesis of iron oxide nanoparticles by sol-gel technique and their characterization,” *IEEE Transactions on Magnetics*, vol. 50, no. 8, pp. 1–4, 2014.
- [60] J. K. Sharma, P. Srivastava, M. S. Akhtar, G. Singh, and S. Ameen, “ $\alpha$ -Fe<sub>2</sub>O<sub>3</sub> hexagonal cones synthesized from the leaf extract of *Azadirachta indica* and its thermal catalytic activity,” *New Journal of Chemistry*, vol. 39, no. 9, pp. 7105–7111, 2015.
- [61] A. Lassoued, B. Dkhil, A. Gadri, and S. Ammar, “Control of the shape and size of iron oxide ( $\alpha$ -Fe<sub>2</sub>O<sub>3</sub>) nanoparticles synthesized through the chemical precipitation method,” *Results in Physics*, vol. 7, pp. 3007–3015, 2017.
- [62] S. Jain, J. Shah, N. S. Negi, C. Sharma, and R. K. Kotnala, “Significance of interface barrier at electrode of hematite hydroelectric cell for generating ecopower by water splitting,” *International Journal of Energy Research*, vol. 43, no. 9, pp. 4743–4755, 2019.
- [63] G. H. Rosenblatt, M. W. Rowe, G. P. Williams Jr., R. T. Williams, and Y. Chen, “Luminescence of F and F<sup>+</sup> centers in magnesium oxide,” *Physical Review B*, vol. 39, no. 14, article 10309, 1989.
- [64] N. Shrivastava, L. U. Khan, Z. U. Khan et al., “Building block magneto-luminescent nanomaterials of iron-oxide/Zn-S@LaF<sub>3</sub>:Ce<sup>3+</sup>,Gd<sup>3+</sup>,Tb<sup>3+</sup> with green emission,” *Journal of Materials Chemistry C*, vol. 5, no. 9, pp. 2282–2290, 2017.
- [65] M. Pal, R. Rakshit, and K. Mandal, “Facile functionalization of Fe<sub>2</sub>O<sub>3</sub> nanoparticles to induce inherent photoluminescence and excellent photocatalytic activity,” *Applied Physics Letters*, vol. 104, no. 23, article 233110, 2014.
- [66] N. Pathak, P. S. Ghosh, S. K. Gupta, R. M. Kadam, and A. Arya, “Defects induced changes in the electronic structures of MgO and their correlation with the optical properties: a special case of electron-hole recombination from the conduction band,” *RSC Advances*, vol. 6, no. 98, pp. 96398–96415, 2016.
- [67] A. Saritha, B. Raju, D. Narayana Rao, A. Roychowdhury, D. Das, and K. A. Hussain, “Facile green synthesis of iron oxide nanoparticles via solid-state thermolysis of a chiral, 3D anhydrous potassium tris(oxalato)ferrate(III) precursor,” *Advanced Powder Technology*, vol. 26, no. 2, pp. 349–354, 2015.
- [68] J. Wu, S. Mao, Z.-G. Ye, Z. Xie, and L. Zheng, “Room-temperature weak ferromagnetism induced by point defects in  $\alpha$ -Fe<sub>2</sub>O<sub>3</sub>,” *ACS Applied Materials & Interfaces*, vol. 2, no. 6, pp. 1561–1564, 2010.
- [69] B. Vallina, J. D. Rodriguez-Blanco, A. P. Brown, L. G. Benning, and J. A. Blanco, “Enhanced magnetic coercivity of  $\alpha$ -Fe<sub>2</sub>O<sub>3</sub> obtained from carbonated 2-line ferrihydrite,” *Journal of Nanoparticle Research*, vol. 16, no. 3, pp. 1–13, 2014.

- [70] A. Lassoued, M. S. Lassoued, B. Dkhil, S. Ammar, and A. Gadri, "Synthesis, photoluminescence and magnetic properties of iron oxide ( $\alpha$ -Fe<sub>2</sub>O<sub>3</sub>) nanoparticles through precipitation or hydrothermal methods," *Physica E: Low-dimensional Systems and Nanostructures*, vol. 101, pp. 212–219, 2018.
- [71] M. Ram, K. Bala, H. Sharma, and N. S. Negi, "Effect of Co doping on the structural and dielectric properties of ZnO nanoparticles," *AIP Conference Proceedings*, vol. 16, article 050104, 2016.
- [72] Y. Badali, Ş. Altındal, and İ. Uslu, "Dielectric properties, electrical modulus and current transport mechanisms of Au/ZnO/n-Si structures," *Progress in Natural Science: Materials International*, vol. 28, no. 3, pp. 325–331, 2018.
- [73] S. Gowreesan and A. Ruban Kumar, "Structural, magnetic, and electrical property of nanocrystalline perovskite structure of iron manganite (FeMnO<sub>3</sub>)," *Applied Physics A*, vol. 123, no. 11, pp. 1–8, 2017.
- [74] S. Sharma, T. Basu, A. Shahee, K. Singh, N. P. Lalla, and E. V. Sampathkumaran, "Complex dielectric and impedance behavior of magnetoelectric Fe<sub>2</sub>TiO<sub>5</sub>," *Journal of Alloys and Compounds*, vol. 663, pp. 289–294, 2016.
- [75] H. Joshi, S. Gowreesan, and A. R. Kumar, "Influences of Ni<sup>2+</sup> on magnetic property and dielectric property in spinel structure of Mg ferrite (Mg<sub>1-x</sub>Ni<sub>x</sub>Fe<sub>2</sub>O<sub>4</sub>)," *Journal of Materials Science: Materials in Electronics*, vol. 29, no. 4, pp. 3449–3457, 2018.
- [76] S. Gowreesan and A. Ruban Kumar, "Effects of Mg<sup>2+</sup> ion substitution on the structural and electric studies of spinel structure of Co<sub>1-x</sub>Mg<sub>x</sub>Fe<sub>2</sub>O<sub>4</sub>," *Journal of Materials Science: Materials in Electronics*, vol. 28, no. 6, pp. 4553–4564, 2017.
- [77] M. C. Dimri, H. Khanduri, H. Kooskora et al., "Room-temperature ferromagnetism in Ca and Mg stabilized cubic zirconia bulk samples and thin films prepared by pulsed laser deposition," *Journal of Physics D: Applied Physics*, vol. 45, no. 47, article 475003, 2012.